SANDIA REPORT

SAND99–8232
Unlimited Release
Printed February 1999

Stress Evaluation and Model Validation Using Laser Ultrasonics

Wei-yang Lu, Jay J. Dike, Lawrence W. Peng, James C. F. Wang

Prepared by
Sandia National Laboratories
Albuquerque, New Mexico 87185 and Livermore, California 94550

Sandia is a multiprogram laboratory operated by Sandia Corporation, a Lockheed Martin Company, for the United States Department of Energy under Contract DE-AC04-94AL85000.

Sandia National Laboratories

Issued by Sandia National Laboratories, operated for the United States Department of Energy by Sandia Corporation.

Available to DOE and DOE contractors from
Office of Scientific and Technical Information
P.O. Box 62
Oak Ridge, TN 37831

Prices available from (615) 576-8401, FTS 626-8401

Available to the public from
National Technical Information Service
U.S. Department of Commerce
5285 Port Royal Rd
Springfield, VA 22161

NTIS price codes
Printed copy: A04
Microfiche copy: A01

SAND99-8232
Unlimited Release
Printed February 1999

Stress Evaluation and Model Validation Using Laser Ultrasonics

Wei-yang Lu
Experimental Mechanics Department

Jay J. Dike
Solid and Material Mechanics Department

Lawrence W. Peng and James C. F. Wang
Materials Chemistry Department
Sandia National Laboratories
P.O. Box 0969
Livermore, CA 94551-0969

ABSTRACT

Rayleigh surface waves can be used to evaluate surface stresses and through-thickness stress gradients based on acoustoelasticity. Laser based ultrasonic techniques, which generate and detect surface waves, have the advantages of good spatial resolution and remote operation. The techniques have many potential applications. This is the final report of a LDRD project that is the first to exploit the benefits of laser ultrasonics for stress and stress gradient evaluation. The approach consists of both simulation and experiments. Finite element analysis has successfully modeled laser ultrasonic generation and propagation, which provide guides for developing experimental techniques and measurements. Experimental measurements on simple geometries with known residual stress along with analytical solutions and simulations provide the means to evaluate spatial and stress resolution of laser ultrasonic techniques. In addition, the texture model adds a new perspective to the theory of acoustoelasticity. The scattering of acoustoelastic coefficient of Al6061-T6 reported in the literature can now be explained by the effect of texture from the texture model described here.

Acknowledgment

The authors thank Chi-Sing Man, Professor of Mathematics, University of Kentucky, for his texture model of acoustoelasticity and his very helpful discussions regarding acoustoelastic theory, and George Johnson, Professor of Mechanical Engineering, University of California, Berkeley, for discussions in finite element modeling and experiments. The authors also like to thank Ken Lee (8746) and Steve Holland (summer student, Cornell University) for their support in conducting the experiments, and Don Sheaffer (8120) for his help in data analysis.

Contents

Figures

Tables

Stress Evaluation and Model Validation Using Laser Ultrasonics

Introduction

The evaluation of mechanical stress has been, and continues to be, an active area of research due to its effect on the performance and reliability of mechanical hardware. Of particular interest is the ability to predict and experimentally verify stress fields in engineering components resulting from both their intended operation (external loading) and fabrication process (residual stress). Non-contact stress measurement techniques are needed for in-situ experimental evaluation of stresses for validation of constitutive models and structural analyses to enable model-based design.

Based on the acoustoelastic behavior of materials, stresses can be determined from ultrasonic wave velocities. Laser Ultrasonics (LU) is a novel method for the optical generation and detection of ultrasound. This report describes the development of techniques for LU measurements of stress and through-the-thickness stress gradients, as well as analytical and numerical models. Experiments are used to validate simulations to qualify this stress measurement technique.

The report includes four major sections: (1) advances in LU experimental techniques; (2) theoretical and experimental investigation of texture effects on the acoustoelastic behavior of metals (e.g., aluminum alloy 6061-T6); (3) modeling transient heating from a laser pulse and the subsequent wave motion using thermal and mechanical finite element codes and its use to guide development of LU techniques; and (4) experiments performed to measure residual stresses and comparing results with model predictions.

Background

The acoustoelastic effect refers to the fact that elastic wave velocities vary with stress. Measurements of the change in stress-induced velocity yield information which leads to the determination of stresses. Some work has been done to explore the possibility of using ultrasonic waves, including bulk longitudinal and shear waves as well as surface waves, for the nondestructive evaluation of stresses. The focus here is on Rayleigh surface waves which have the advantage of applicability to evaluating both surface stresses and stress gradients.

Theoretically, the ultrasonic approach can be applied to any solid. In addition to metallic materials, it is also applicable to polymers and glasses. Previous work on ultrasonic stress evaluation has been restricted to narrow band generation and single wave modes using piezoelectric (PZT) or electromagnetic acoustic transducer (EMAT) technology [1 – 5]. PZT transducers require a couplant whereas EMATs are technically non-contact but need to be placed in close proximity to the specimen surface. Both

techniques have limited spatial resolution due largely to the physical size of the transducer. Laser induced and detected ultrasound is less burdened by such physical constraints. Long laser beam coherence lengths allow for remote operation while generation and detection areas are typically much smaller than 1 mm^2. The limiting factor instead becomes the precision to which time-of-flight (TOF) measurements can be made. This places limits on source to detector spot spacings. Other ultrasonic techniques have been developed to improve the spatial resolution. Sharp edge wedges are usually bound to the pick-up piezoelectric transducers, known as the Rayleigh or surface wave device (SWD), to provide a better spatial resolution when the stress field is not uniform. The smallest distance reported is 11 mm. Acoustic miscroscopes (AM) can measure localized stress for a very small area, from 30 μm to 2 mm [6, 7]. Both SWD and AM methods may lack the flexibility required for general applications. The advantages of laser ultrasound are convenience, freedom from radiation hazards, and wide applicability.

Ultrasonic techniques do have difficulties. One is the smallness of the acoustoelastic effect, in which stresses induce only very small velocity changes (for example, the relative change of wave speed for aluminum is about 10^{-5} MPa^{-1}). This leads to challenging experimental and theoretical problems. A precision of 1 part in 10^5 or higher is required for the measurement of wave speeds. In addition, other competing factors (e.g. the weak anisotropy of the material) which are usually ignored in the engineering application of elasticity can no longer be neglected in acoustoelasticity.

Equations of Acoustoelasticity

Consider a plate and a spatial coordinate system with its 1-, 2-, and 3-axes falling in the rolling, transverse, and normal directions of the plate, respectively. Suppose the plate is orthotropic and carries in-plane stresses σ_1 and σ_2. Let V_1 and V_2 be the speed of Rayleigh surface waves propagating in the 1- and the 2- directions, respectively. Let V_1° and V_2° be the corresponding Rayleigh wave speeds when the plate is unstressed. Under the assumptions that the plate is slightly anisotropic and that both the plate and the initial stress is homogeneous

$$\Delta V_1 / V_1^\circ = K_{11}\,\sigma_1 + K_{21}\,\sigma_2, \quad \Delta V_2 / V_2^\circ = K_{12}\,\sigma_1 + K_{22}\,\sigma_2, \tag{1}$$

where $\Delta V = V - V^\circ$ and K_{ij} (i, j = 1, 2) are acoustoelastic coefficients. Since rolled aluminum plates are usually textured, the four acoustoelastic coefficients in (1) are generally distinct and $V_1^\circ \neq V_2^\circ$. The texture-induced anisotropy has been customarily ignored. For an isotropic plate, we have

$$K_{11} = K_{22}, \quad K_{12} = K_{21}, \quad V_1^\circ = V_2^\circ = V_R, \tag{2}$$

where V_R is the Rayleigh-wave speed for the unstressed isotropic medium. The values of K_{ij} are obtained experimentally.

When the stress varies in the direction of depth x_3, the Rayleigh wave will be dispersive (wave velocity depends on wave length) since the depth of penetration of the

Rayleigh wave is proportional to the wavelength. Consider a uniaxial, linear stress distribution in the 3-direction [1]

$$(v_1 - v_R) / v_R = k_1 \sigma_1 + (\beta_1 / \omega)(d \sigma_1 / d x_3) \quad (3)$$

where $\omega = 2\pi f$ denotes circular frequency, and β_1 is a constant. The stress gradient can be determined by measuring the Rayleigh wave velocity at two different frequencies f1 and f2

$$((v_1)_{f1} - (v_1)_{f2}) / v_R = b (d \sigma_1 / d x_3) \quad (4)$$

where $b = \beta_1 (1/\omega_1 - 1/\omega_2)$.

Experimental Setup

The experimental setup consists of three parts: the LU system for generating and detecting ultrasonic waves, the data acquisition and analysis system to measure the time-of-flight (TOF) of a wave between two points, and the mechanical system for loading samples.

A schematic of a typical LU setup is shown in Figure 1. A pulsed laser generates ultrasonic waves by rapidly heating a point (or a line) on the sample. The excitation laser is a pulsed, frequency-doubled, Q-switched Nd:YAG operating at 10 Hertz (Hz), with a pulsewidth of approximately 10 nanoseconds (ns) at 532 nanometers (nm). The detection laser is a continuous-wave (CW), frequency-doubled, diode pumped Nd:YAG laser emitting at 532 nm.

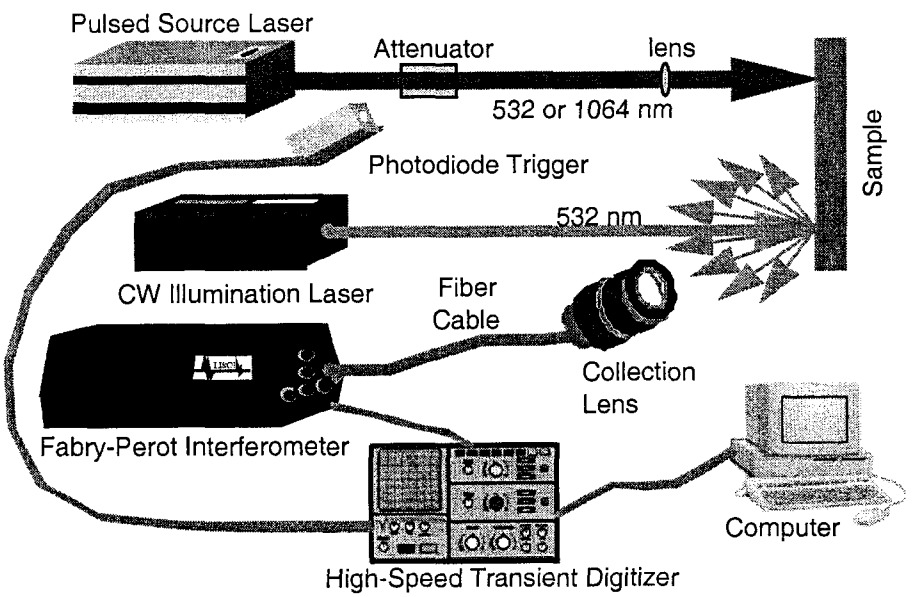

Figure 1. A schematic of LU and data acquisition setup.

The CW laser illuminates a point on the sample. The reflected light is collected via a camera lens, and focused onto a fiberoptic which is connected to the input of an UltraOptec LISOR Fabry-Perot interferometer. Surface displacement normal to the surface is detected. Extraneous scattered light from other sources (primarily the excitation laser) is minimized by using a spatial filter placed in front of the camera lens and using beam blocks placed at various locations.

The data acquisition and analysis equipment is also shown in Figure 1. The signal from the interferometer is digitized at 1 GHz by a high-speed transient digitizer (TEK RTD720), which is then stored and analyzed by a computer.

Figure 2 shows a picture of a custom made loading frame with a tensile specimen in place. The loading frame, which is screw driven, is mounted on x-y-θ_Z stage, so we can make various LU measurements without disturbing the stress state of the sample or the optical paths. Loading is applied manually by turning the screw with a wrench.

A second loading frame used for tensile tests is shown in Figure 3. This frame is fastened on the optical table directly and not as versatile as the previous one, but allows larger specimen size and better alignment for a more precise measurement. The position of the sample is fixed.

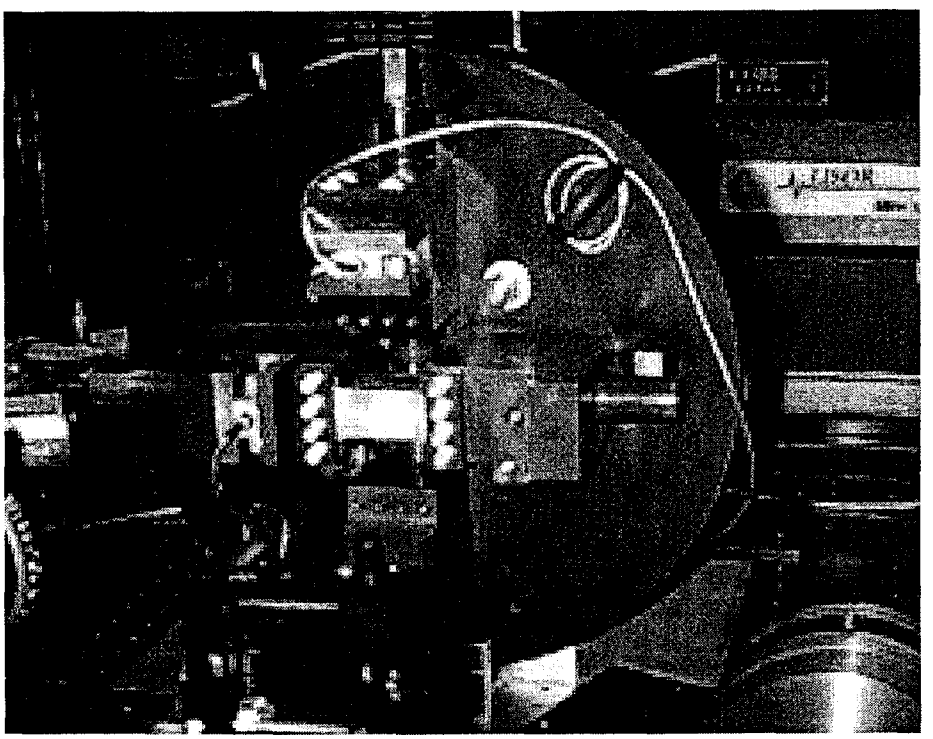

Figure 2. A tensile loading system mounted on x-y-θ_Z stage.

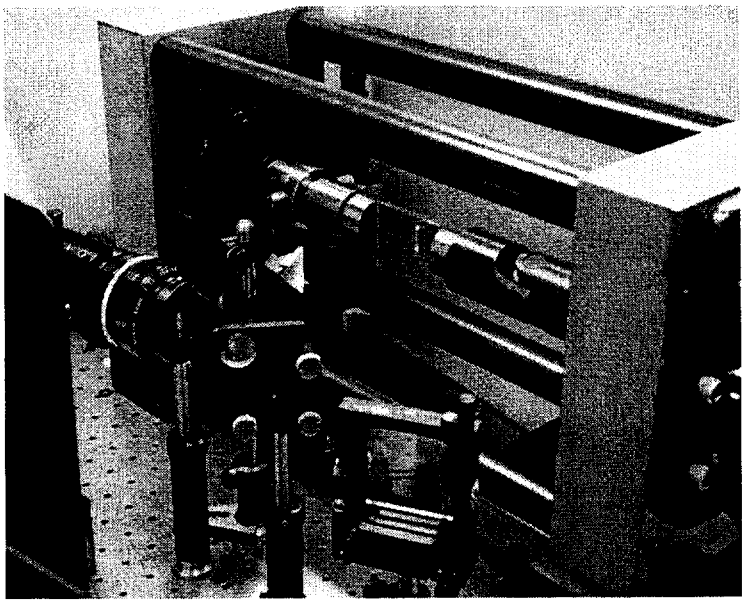

Figure 3. A tensile loading system with 10 kips capacity.

Advances in LU Experimental Techniques

The LU system shown in Figure 1 is a typical single beam excitation and single point detection scheme. Techniques of ultrasonic generation and detection and signal processing were developed to meet the needs of stress evaluation.

Two-point Detection Method

One drawback of the single point detection method is that the jitter from the trigger signal, from either the synchronized output of the pulsed laser or the photodiode trigger, causes inconsistent time-of-flight (TOF) results. To eliminate the problem of jitter caused by the trigger signal, a two-point detection method was developed. As shown in Figure 4, the detection beam is reflected twice from the sample and then fed to the interferometer. The interferometer output waveform is the sum of waveforms at two points, which behaves as if there are two receivers although only one interferometer is used. TOF can be accurately determined between the two measurement points, instead of relative to the excitation laser pulse. This two-point detection method requires a mirror-like surface finish at the reflection points.

Narrow band generation

Laser ultrasound generated using a single beam is generally broad band. There is very limited control of the frequency content of the signal. One goal of the multi-beam

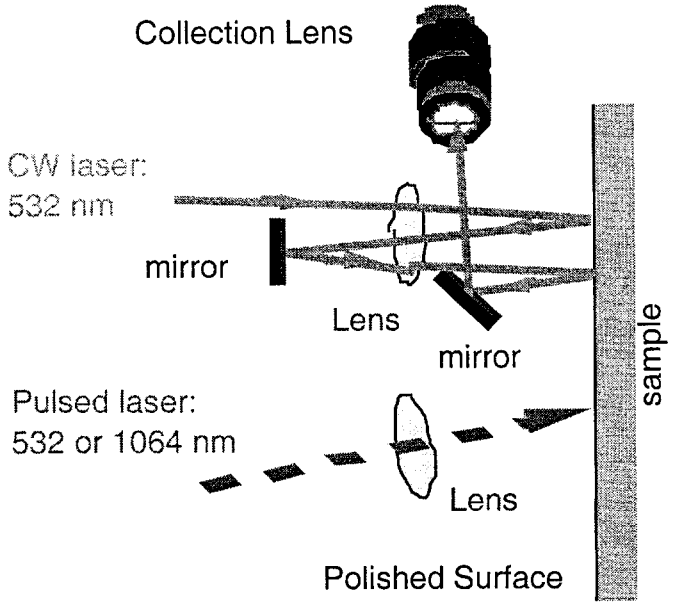

Figure 4. Two point detection method.

technique was to enable the generation of narrow band ultrasound [8]. Simulations had shown that multi-beam excitation could give ultrasonic signals with well-defined Fourier Transforms. This is relevant since we are interested in measuring small shifts in the Fourier Transform. A schematic of the experimental arrangement for multi-beam experiments is shown in Figure 5.

Multiple beams were generated by using a binary optical grating from MEMS Optical, Inc. With these gratings, the input laser beam could be split into 8 beams with fairly uniform intensity (typically the same within a few percent) per beam. In practice, we used the internal 6 beams, as the outer two were often substantially weaker in intensity and less well-defined.

The excitation laser output is approximately one-half inch in diameter and is focused (using a two inch f/2 bi-convex lens) slightly behind the binary optical grating (BOG). This gave the best definition of multiple beams, and minimized laser damage to the BOG. The multiple laser beams were collimated (using a two inch f/2 plano-convex lens) to a diameter of approximately one-half inch using the plano-convex lens, and then focused onto the sample using the cylindrical lens (two inch f/3.5). The cylindrical lens was mounted on a translation stage, and oriented so that focusing occurred in the horizontal direction.

Scattered detection laser light from the sample is collected via a camera lens, and focused onto a fiberoptic cable which is connected to the input of a UltraOptec LISOR Fabry-Perot interferometer. Extraneous scattered light from other sources (primarily the excitation laser) is minimized by using a spatial filter placed in front of the camera lens and using beam blocks placed at various locations.

For single beam excitation, the experimental arrangement is the same except that biconvex and plano-convex lenses, and the BOG were removed.

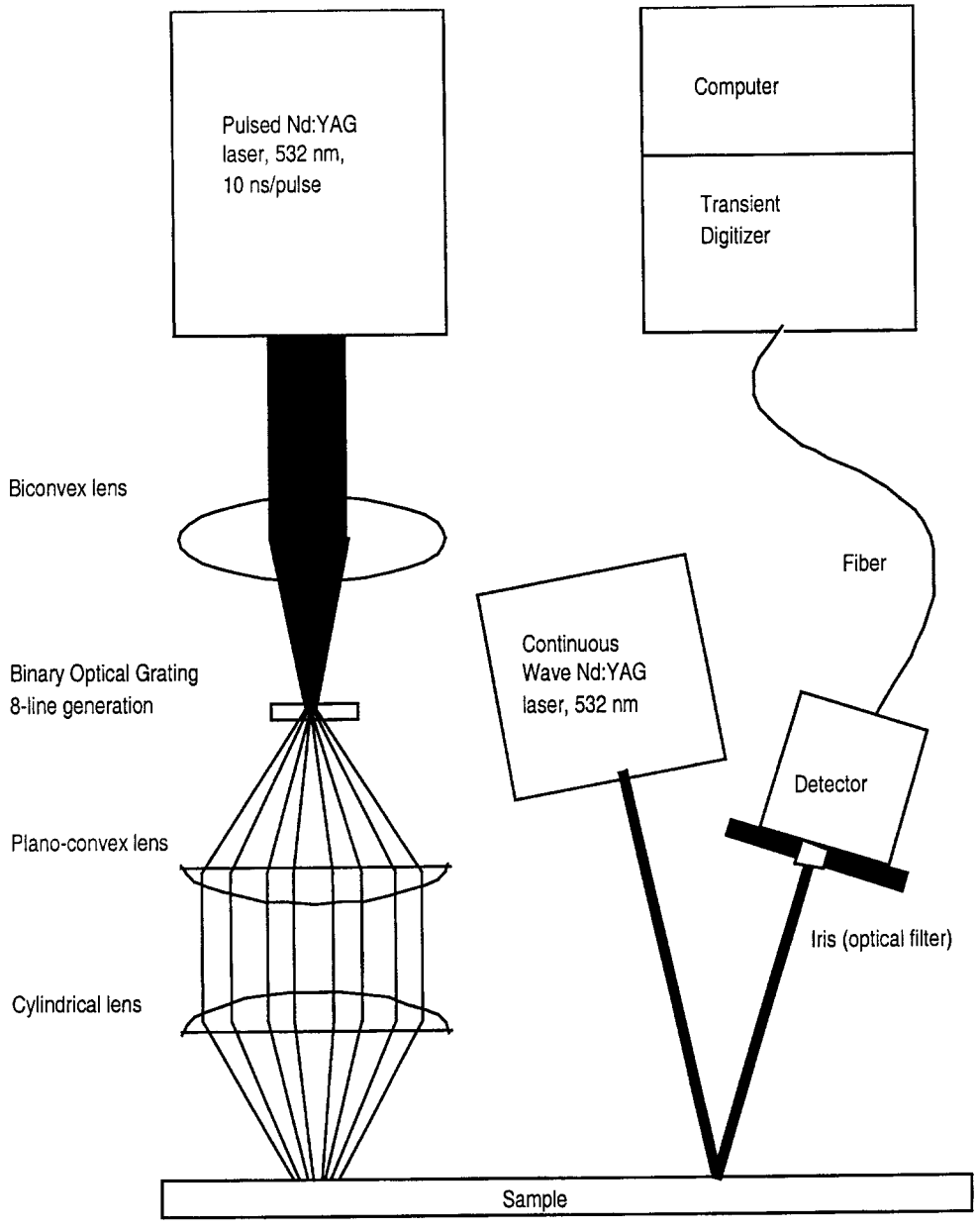

Figure 5. Multi-beam excitation configuration.

RESULTS

Experiments were performed on both flat plate and pipe samples (aluminum). The experiments for the pipe were set up to detect ultrasonic waves traveling around the circumference of the pipe.

In order to establish the viability of multiple beams, we used a flat aluminum sample with a polished surface. The specular reflection of the detection laser had the same circular geometry as the incident laser beam. The cylindrical lens was initially placed approximately 7.5 inches away from the sample, and then moved towards the sample. The optimum position of the cylindrical lens is determined by examining the Fourier Transform of the obtained ultrasonic signal.

Once established using the flat surface, the technique was applied to the aluminum pipe. The pipe surface was polished to give a linear specular reflection. The excitation and detection laser beams were aligned circuferentially. Figures 6, 7, and 8 show ultrasonics signals obtained using the pipe sample. Figure 6 is a multi-beam signal at a non-optimal position, Figure 7 is a multi-beam signal at the optimal position, and Figure 8 is the single beam signal at the same position that the optimal multi-beam signal was obtained.

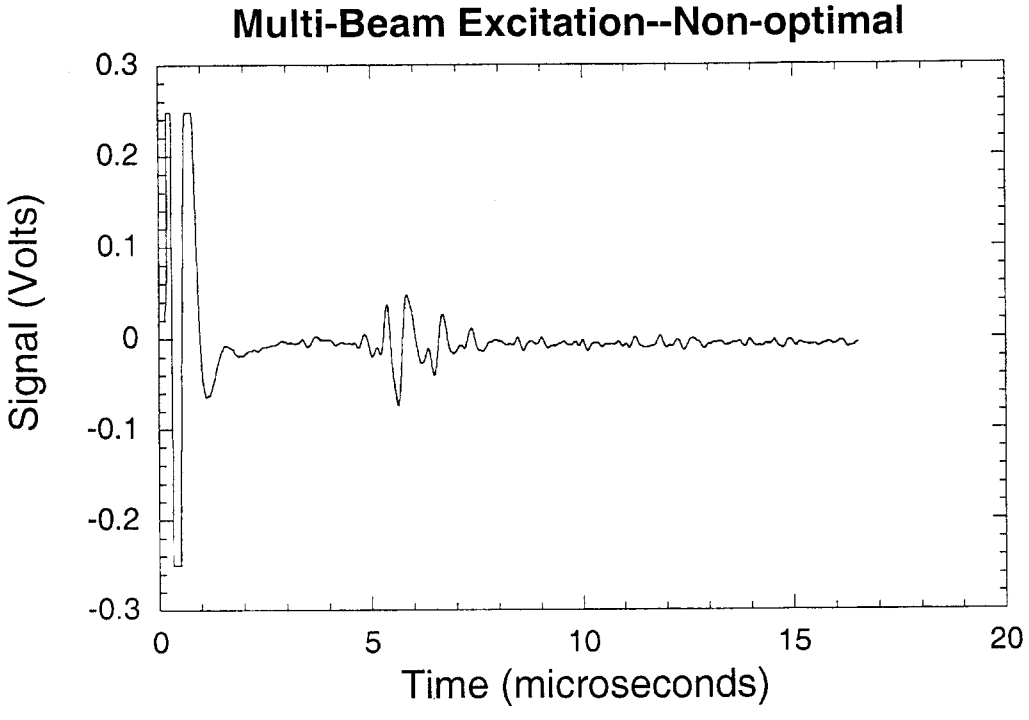

Figure 6. A multi-beam signal at a non-optimal position.

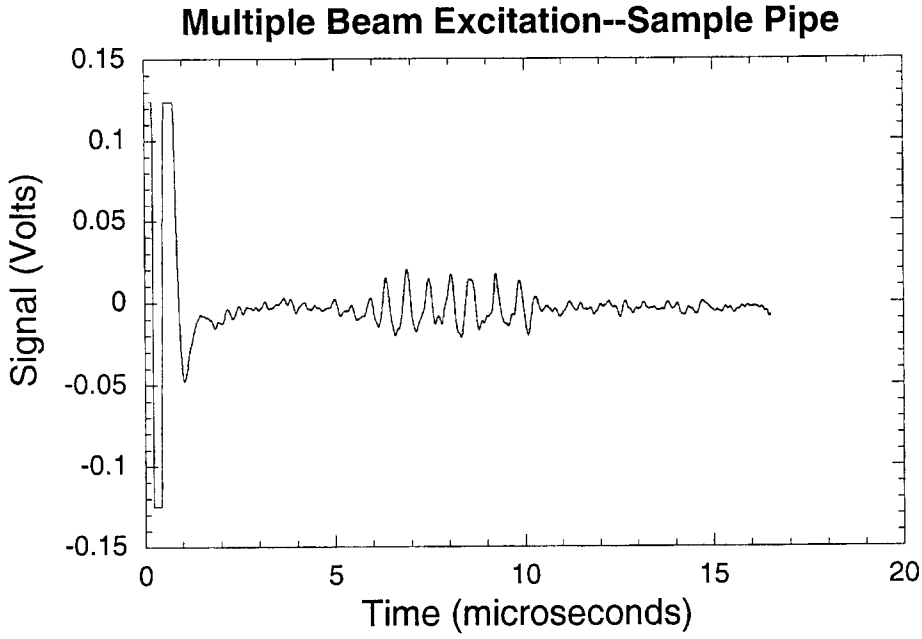

Figure 7. A multi-beam signal at the optimal position.

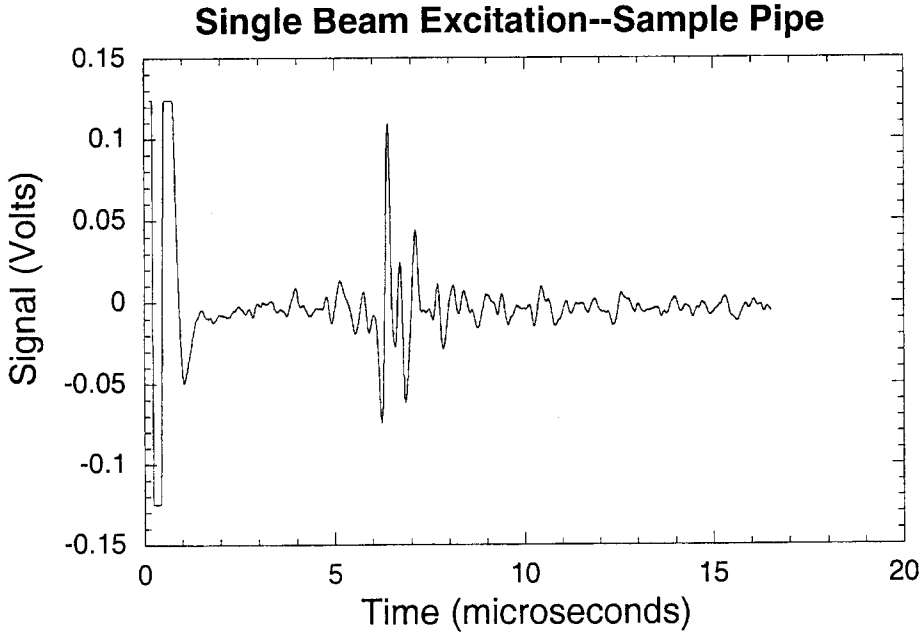

Figure 8. The single beam signal at the same position that the optimal multi-beam signal was obtained.

Figure 7 clearly shows an optimal setting with well-defined oscillations corresponding to the individual excitation laser beams. When the grating is removed, and the equivalent single beam experiment performed, the signals are characterized by a strong initial pulse followed closely by a couple of weak oscillations which quickly degrade into noise. The same is basically true when using the multi-beam setup, but taking data at a non-optimal position.

Figures 9, 10, and 11 show the associated Fourier Transforms. As can be seen, the bandwidth of the optimized multiple beam excitation are the narrowest and cleanest. In the optimal case, the Fourier Transform peaks at 1.82 MHz. Even at the optimal position of excitation and detection, when using a single beam, the bandwidth increases significantly. Likewise, when multi-beam excitation is used at non-optimal positions, the waves interfere sufficiently so that single and multi-beam excitation appear very similar. The Finite Element Modeling section also shows the effectiveness of multiple sources for generating narrow band signals.

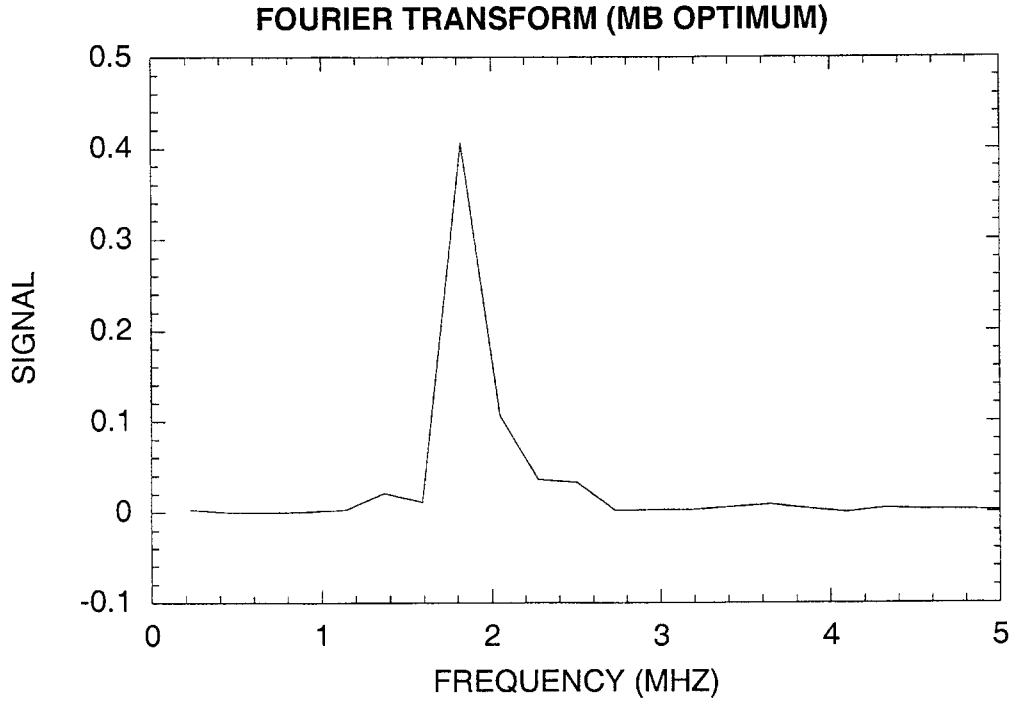

Figure 9. Fourier Transform of a multi-beam signal at the optimal position.

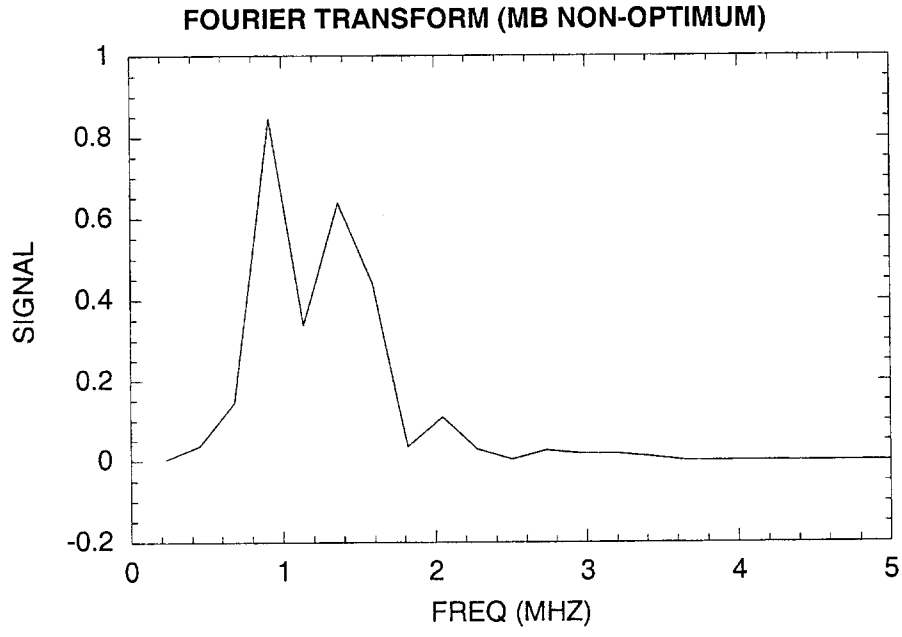

Figure 10. Fourier Transform of a multi-beam signal at the non-optimal position.

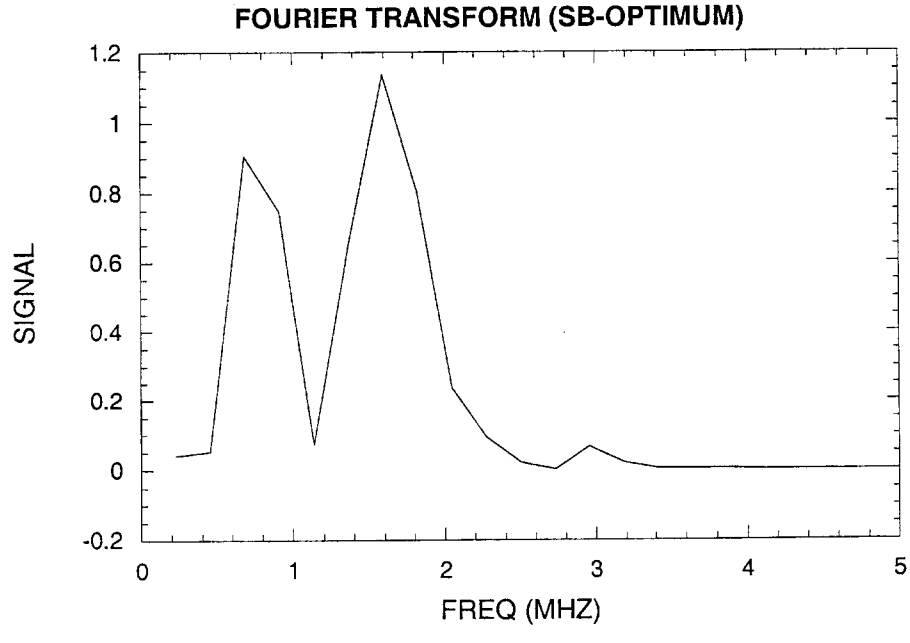

Figure 11. Fourier Transform of a single-beam signal at the optimal position.

Time-Of-Flight (TOF) Measurement

A LabVIEW virtual instrument (VI) was developed to control data acquisition and to calculate TOF. Figure 12 shows a typical LU waveform from a two-point detection scheme. Two arrival signals are similar. The VI allows repetitive measurement, record averaging and saving, and TOF display. The TOF was calculated by the cross correlation of two signals [9]. MatLab programs were also developed for post-experiment signal processing and analysis.

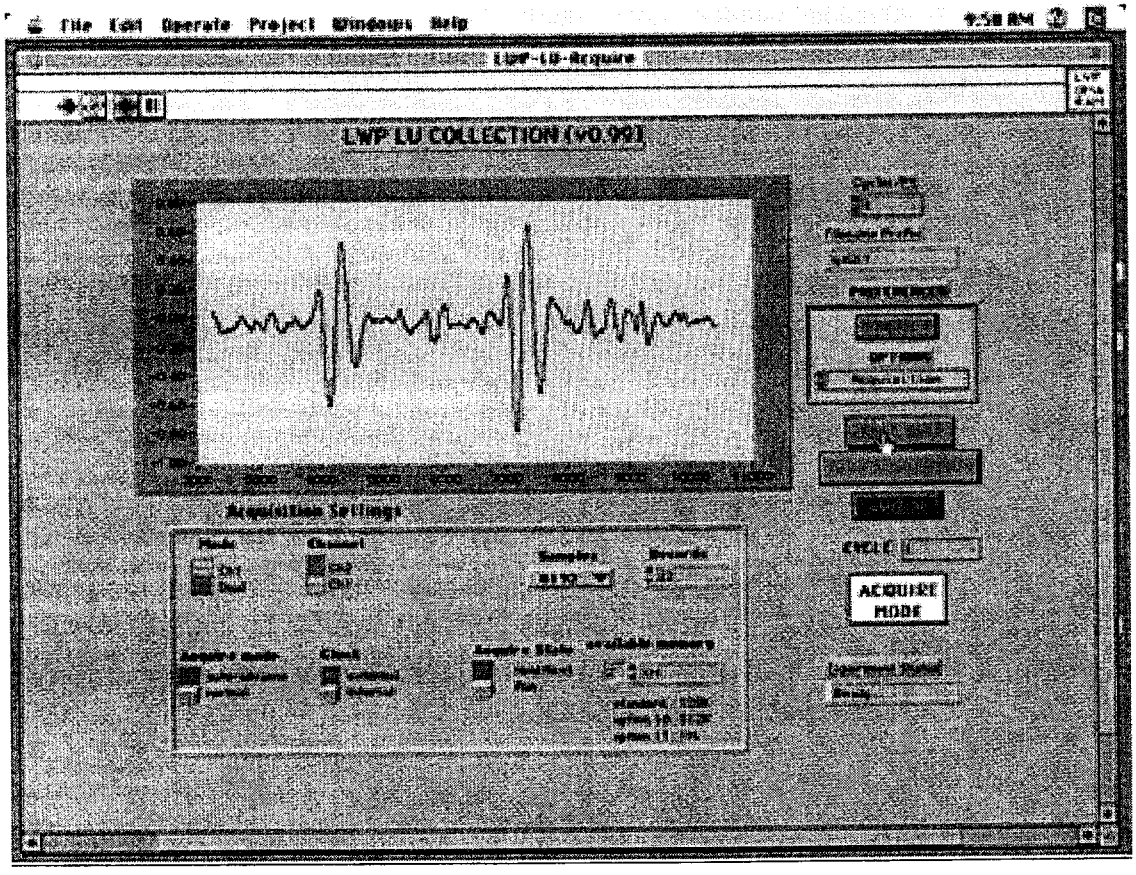

Figure 12. The panel of the LabVIEW VI and a typical waveform of two-point detection.

Acoustoelastic Coefficients of Al6061-T6

In the literature, the assumption of material isotropy is commonly adopted and measured values of K_{ij} have been reported for steels and aluminum alloys. We used the LU technique to measure the acoustoelastic coefficients of Al6061-T6. The LU technique had not been used for acoustoelastic measurement before.

Acoustoelastic Experiments

Experiments were performed using the loading frame shown in Figure 2. The thickness of the tensile specimen was 3.18 mm (1/8"). The gage length was greater than 76 mm (3"). Figure 13(a) shows the schematic of a K_{11} measurement. An ultrasonic wave, generated by a line excitation, travels along the axis of loading to receiver 1 (R1) and then to receiver 2 (R2). Since there is no transverse loading ($\sigma_2 = 0$) and the distance between R1 and R2 was fixed, the first equation of (1) becomes

$$\Delta t_1 / t_1^{\circ} = - \Delta V_1 / V_1^{\circ} = - K_{11} \sigma_1, \tag{5}$$

where t_1 is the TOF from R1 to R2.

The relative changes in the surface wave velocity measured from uniaxial tensile tests of aluminum alloy 6061-T6 are shown in Figure 14. Experiments were repeated under various measuring conditions as listed in Table 1. Consider the 'wf' experiment, the distance d between two receiving points was 15 mm; the TOF was the average of 20 measurements; each TOF was determined from the average of 32 waveform records. When the time was determined with only one TOF measurement, such as wa, wb and wc,

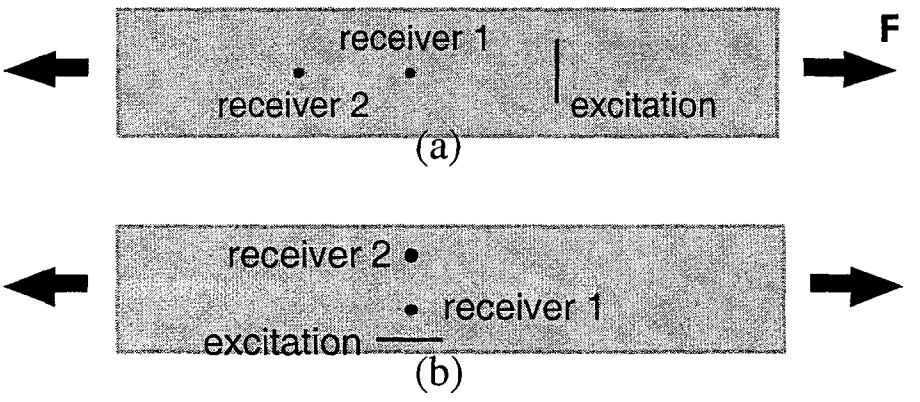

Figure 13. Schematics of K_{11} and K_{12} measurement.

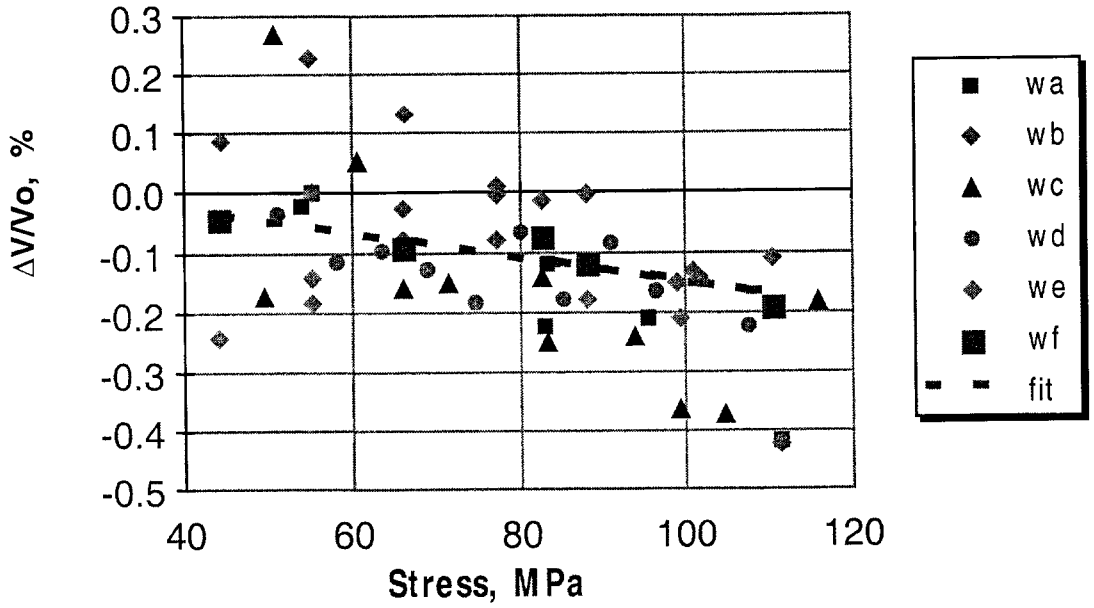

Figure 14. Acoustoelastic effect of Al6061-T6. The loading of experiments wa through wf was the same but different data acquisition parameters were used, which are listed in Table 1.

Table 1. Acoustoelastic coefficient K_{11} obtained from LU measurements

Experiment	d, mm	# of TOFs	# of Records	K_{11} (GPa^{-1})
wa	9	1	64	-0.075
wb	9	1	64	-0.037
wc	9	1	64	-0.047
wd	15	3	32	-0.019
we	15	3	32	-0.032
wf	15	20	32	-0.022

Table 2. Some measured values of Rayleigh wave K_{11} and K_{12} for aluminum alloys.

Al Alloy	Exp Tech	K_{11} (GPa^{-1})	K_{12} (GPa^{-1})	Reference
A2017T3	AM	-0.024	0.0074	[10]
6061-T6	AM	-0.019	0.0070	[7]
6061-T6	EMAT	-0.029		[11]
B95T	SWD	-0.033		[12]
6061-T651	SWD	-0.012	0.0088	[13]
2024-T351	SWD	-0.011	0.0075	[14]
6061-T6	SWD	-0.017		[15]
6061-T6	LU	-0.022		[16]

the scatter is larger than the acoustoelastic effect. It is known that LU has a lower sensitivity compared to the conventional piezoelectric technique. A large number of averages is needed to improve the signal-to-noise ratio. The wf data has the least amount of scattering and was fitted by the dashed line in Figure 14.

A comparison with previously determined results of aluminum alloys from various investigators and techniques is listed in Table 2. The range of values in K_{11} is striking. Should one value within this range be chosen arbitrarily as the acoustoelastic constant K_{11} in the velocity shift formula, equation (1), an error of over 100% in the prediction of σ_1 could easily result if we use Rayleigh waves to evaluate stress in a particular sample of aluminum alloy. A reason for the variations apparent in Table 2 is given in the next section and helps one to determine what value of the acoustoelastic constant is appropriate for a given application.

Variations in the K_{11} values of aluminum alloys have been variously speculated to be due to the effects of dislocations, texture, or penetration depth, often by authors who tried to explain why their measured value was quite different from what had been reported previously in the literature for the same alloy. Some pioneering theoretical and experimental studies [17-19] suggested that for aluminum alloys crystallographic texture might profoundly influence acoustoelastic coefficients of bulk waves. Here we investigate how and to what extent crystallographic texture affects the acoustoelastic coefficients K_{11} and K_{12} of Rayleigh waves in aluminum alloys.

Effects of Crystallographic Texture

Recently a general constitutive equation in acoustoelasticity has been derived [20] for weakly-textured orthorhombic aggregates of cubic crystallites. Besides the initial stress, this constitutive equation contains seven texture coefficients and twelve material constants. Two micromechanical models [21] are currently available to estimate all twelve material constants from the second-order (SOEC) and third-order elastic constants (TOEC) of the constituting crystallites. With the constitutive equation in hand and the material constants for polycrystalline aluminum estimated, we can follow the standard procedures in continuum mechanics to find the wave velocities and derive formulae for the acoustoelastic coefficients. These formulae, which give the acoustoelastic coefficients as affine functions of the seven texture coefficients, show quantitatively how crystallographic texture would affect the values of the acoustoelastic coefficients.

Two micromechanical models, namely the Man-Paroni model (MP) and the generalized Voigt model (GV), are currently available to estimate the twelve material constants form SOEC and TOEC of the constituting crystallites. Using the SOEC and TOEC for aluminum single crystals at 25°C as reported in [22, 23], the values of twelve material constants can be calculated. Using these material constants, the MP model predicts [24]

$$K_{11} = -0.0135 - 0.1334\,W_{400} + 0.1548\,W_{420} + 0.0920\,W_{440} + 0.6945\,W_{600} - 1.2918\,W_{620} + 0.9106\,W_{640} + 0.2304\,W_{660}, \quad (6)$$

$$K_{12} = 0.0091 + 0.1010\,W_{400} + 0.2192\,W_{420} - 0.0509\,W_{440} + 0.1775\,W_{600} + 0.1211\,W_{620} - 1.024\,W_{640} + 0.2304\,W_{660}, \quad (7)$$

where W_{lmn} are texture coefficients. The GV model gives

$$K_{11} = -0.0137 - 0.1002\,W_{400} + 0.1187\,W_{420} + 0.1047\,W_{440} + 0.6943\,W_{600} - 1.2914\,W_{620} + 0.9104\,W_{640} + 0.2304\,W_{660}, \quad (8)$$

$$K_{12} = 0.0095 + 0.0321\,W_{400} + 0.1475\,W_{420} - 0.0796\,W_{440} + 0.1774\,W_{600} + 0.1211\,W_{620} - 1.024\,W_{640} + 0.2304\,W_{660}, \quad (9)$$

Experiments were performed to verify the effect of texture on the acoustoelastic coefficients K_{11} and K_{12} of aluminum alloy 6061-T6.

Experimental Validation of Texture Models

We prepared two Al6061-T6 specimens. After the samples were machined, acoustoelastic measurements were made on Specimen 1 and 2 after a 0 and 0.7% (Figure 15) plastic deformation, respectively. Experiments were similar to tests described earlier. Both K_{11} and K_{12} were measured as shown in Figure 13. The load frame shown in Figure 3 was used in this study. As shown in the figure, a specimen is under loading, and it pertains to the configuration for K_{12} measurement. Two laser spots, i.e., the two receiving points, can be seen on the specimen. The specimen is under uniaxial tension in the 1-direction, i.e. $\sigma_1 = F/A$, where F is the tensile load and A the original cross-sectional area, and $\sigma_2 = 0$. The width, thickness, and length of the gage section of specimens were 38 mm, 4 mm, and 100 mm, respectively. The distance between two receivers was about 12 mm. The wavelength of the Rayleigh waves in question was estimated to be about 1.5 mm.

The loading during K_{11} and K_{12} measurements were all elastic, i.e., the specimens were not loaded beyond yield stress. We assume that the textures of the samples remain unchanged during the elastic loading. Measurements were repeated at least once. A typical $\Delta V_i / V_i^\circ$ (i = 1, 2) vs σ_1 plot for Specimen 1 is shown in Figure 16. The K_{12} data shows a larger scatter. This may be due to the shorter path length between the two receivers, which is limited by the width of the specimen.

After the ultrasonic experiments, the specimens were sectioned, and the texture coefficients of the samples were measured by X-ray diffraction. Measurements were made at the surface and at the middle section (i.e., at half-thickness) of the plate. The results of the X-ray measurements are given in Table 3. Note that the W_{lmn} coefficients measured at the surface of the samples are different from those measured at the mid-section. In particular, Specimen 2, which had undergone plastic deformations, had

significantly different values of W_{420} and W_{440} at its surface. For each specimen, the average of the two X-ray measurements is used in computing the predicted values of K_{11} and K_{12} by the two models. The predicted and measured values of K_{11} and K_{12} for the two samples are displayed in Table 4.

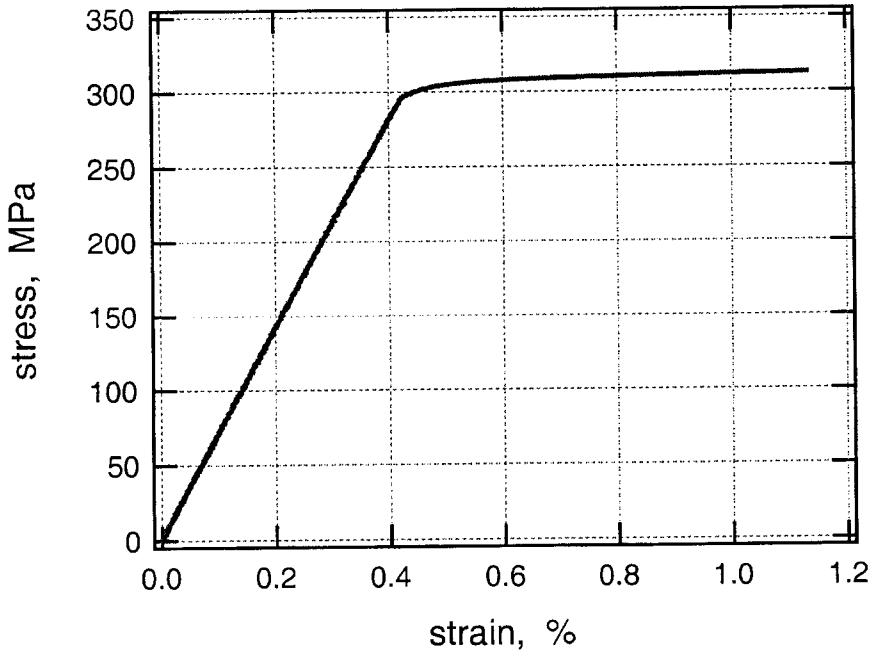

Figure 15. Stress-strain curve of Specimen 2, which was plastically deformed.

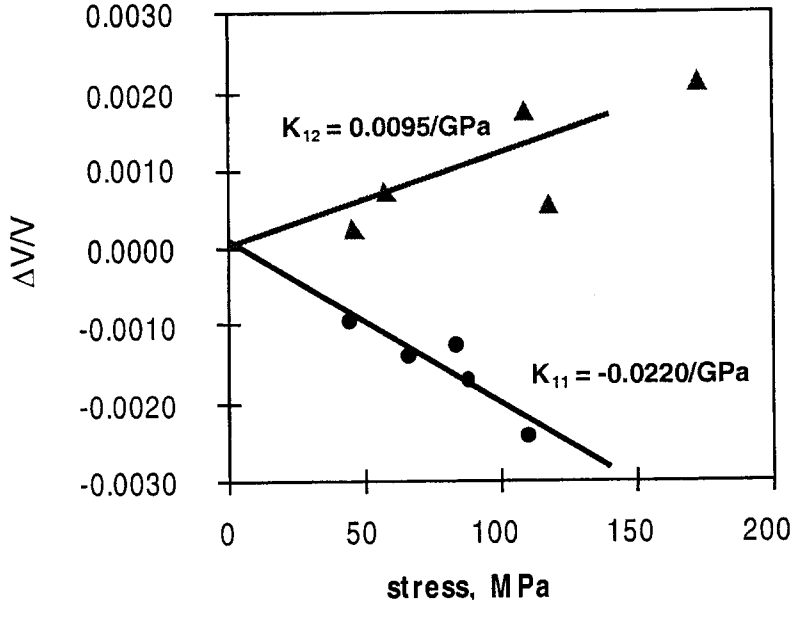

Figure 16. Acoustoelastic effect of Specimen 1, Al6061-T6.

Table 3. Texture coefficients of two samples of aluminum alloy 6061-T6.

Texture	Specimen 1		Specimen 2	
Coefficient	Center	Surface	Center	Surface
W_{400}	0.00095	0.00159	0.00302	0.00398
W_{420}	-0.00344	-0.00368	-0.00285	0.00084
W_{440}	0.00311	0.00175	0.00209	0.00020
W_{600}	-0.00248	-0.00529	-0.00433	-0.00314
W_{620}	0.00229	0.00348	0.00274	0.00335
W_{640}	-0.00200	-0.00299	-0.00330	-0.00352
W_{660}	0.00240	0.00197	0.00278	0.00288

Table 4. Comparison of predicted and measured values of the Rayleigh-wave acoustoelastic coefficients K_{ij} and K_{i2} for two samples of Al6061-T6.

Specimen	Acoustoelastic	Measured			Predicted	
	coeff. (GPa^{-1})	I	II	Avg.	MP	GV
1	K_{11}	-0.023	-0.022	-0.023	-0.022	-0.022
	K_{12}	0.012	0.0095	0.011	0.011	0.011
2	K_{11}	-0.026	-0.016	-0.021	-0.023	-0.023
	K_{12}	0.012	0.0063	0.009	0.013	0.013

A glance at Table 4 reveals that the two models give practically identical predictions for the samples in question. For Specimen 1, the prediction for both K_{11} and K_{12} agrees well with the measured values. For Specimen 2, which had undergone a 0.7% plastic deformation before measurements of the acoustoelastic coefficients were made, the predicted value of K_{11} is about 40% off. On the other hand, we note that the measured acoustoelastic constants of Specimen 2 are themselves not consistent between the two measurements. These measurements were made at the same general area but not exactly at the same place. After Specimen 2 underwent plastic deformation, we observed that its surface became wrinkled, which was then polished to smoothness for LU measurements. The non-uniform deformation might have contributed to the inconsistent values from the two measurements.

On the whole, we can say that the predicted values of K_{11} and K_{12} are in good agreement with the results of measurements on the two samples of Al6061-T6. Also, as given in equations (6) and (8), the two micromechanical models give an average

prediction of K_{11} = -0.0136 / GPa for an isotropic aggregate of aluminum crystallites. In this light, the value of K_{11} = -0.011 / GPa as reported in [14] certainly cannot be regarded as an out-layer. Thus we conclude that crystallographic texture could have a profound effect on the acoustoelastic coefficient K_{11} of Al6061, to the extent that variations such as those displayed in Table 2 could possibly be attributed to the effect of texture alone.

Through-thickness Stress Gradient Experiment

Based on equation (4), a bending test was conducted to demonstrate the feasibility of stress gradient evaluation and to measure the coefficient b. The four-point bending setup is shown in Figure 17. The beam was supported at locations A and D, and the loading was applied at B and C. Within section BC, the bending moment was uniform and it generated a uniform stress gradient field. Beam thickness and width are 3.18 mm (1/8") and 22.2 mm (7/8"), respectively. Although the technique of generating narrow-band ultrasonic signals using LU had been demonstrated, improvements were required so it could be used in practical application. To bypass this difficulty, longitudinal-wave piezoelectric transducers, f1 = 2.25 MHz or f2 = 5.0 MHz, were mounted on a wedge to generate surface waves. The wedge was fastened on the beam using rubber band; transducers could be attached and detached from the wedge. LU was used in detection only. TOF was measured using the two-point detection scheme; so even if the position of the wedge was disturbed during changing transducers, it did not effect $((t_1)_{f2} - (t_1)_{f1}) / t_o$ or $((v_1)_{f1} - (v_1)_{f2}) / v_R$. Figure 18 shows typical signals of bend beam measurement. The signals were taken at a through-thickness stress gradient $d\sigma_1/dx_3$ = 240 MPa/mm.

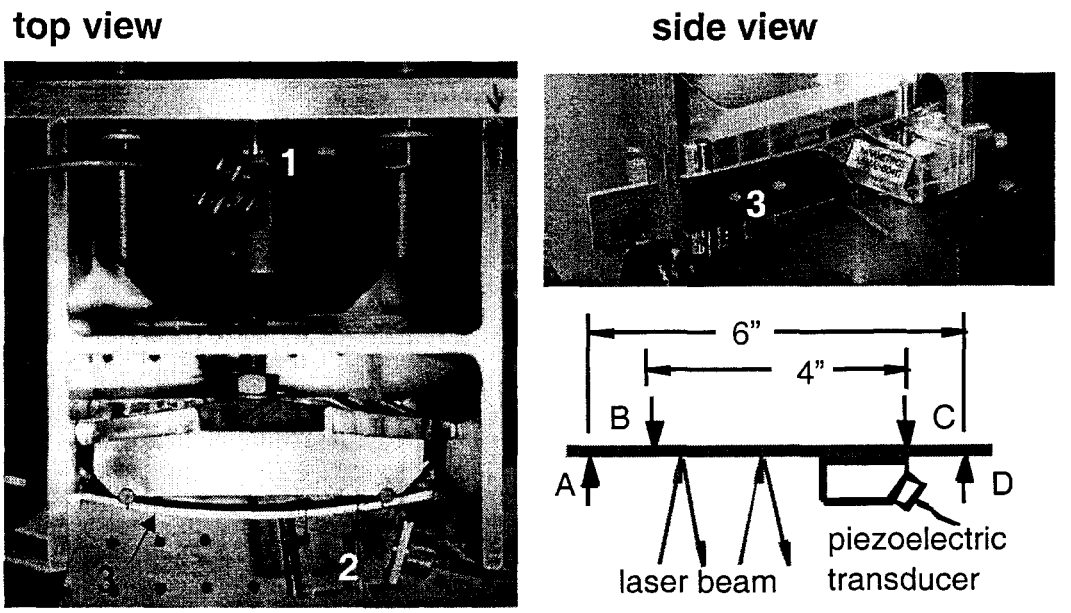

Figure 17. The four-point bending setup. (1) Load cell, (2) piezoelectric transducer and wedge adapter, (3) beam specimen.

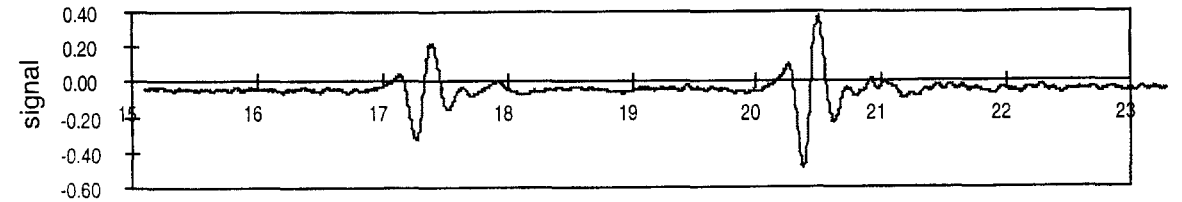

(a)

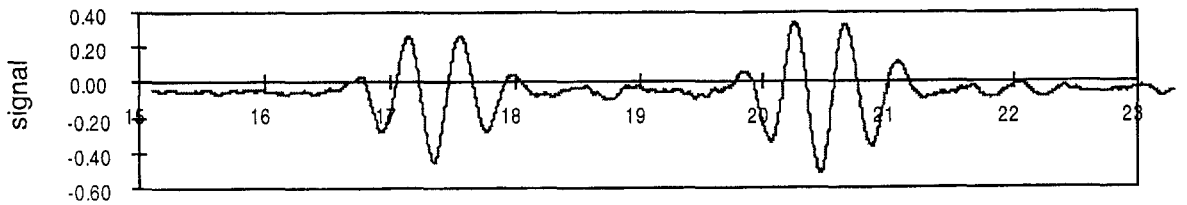

(b)

Figure 18. Typical signals of bend beam measurement, (a) 5 MHz, (b) 2.25 MHz. The signals were taken at a through-thickness stress gradient $d\sigma_1/dx_3 = 240$ MPa/mm.

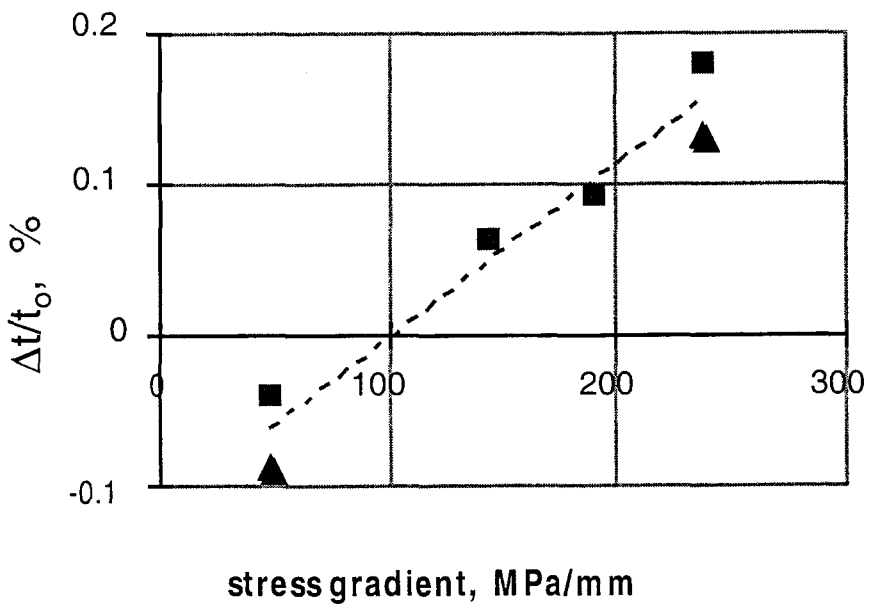

Figure 19. The results of the bending test show the relationship between relative time changes between 2.25 and 5 MHz surface waves and stress gradient (square: first loading, triangle: second loading).

The result of the bending test is shown in Figure 19. The square and triangular marks represent the first and second loading paths of the experiment, and the specimen is completely unloaded between two paths. The dotted line is the best fit of the experimental data. The value Δt is the relative time change of two different frequencies traveling on the same wave path, $\Delta t = t_{5.0MHz} - t_{2.25\ Mhz}$. We made LU measurements on the tension side of the beam. The surface stress is uniform, which is $\sigma_{surface} \approx 1.6\ (d\sigma/dz)$ MPa. Since the 2.25 MHz wave has a longer wavelength and penetrates deeper into the surface, the average stress of the affected layer is lower than that of 5.0 MHz wave. According to equation (1) and the negative k_{11} value, the 2.25 MHz wave has a faster velocity (or shorter TOF). This is consistent with the experimental results. Ideally, the line should pass the origin. It is possible that there are residual stresses due to surface preparation. This needs further investigation.

Finite Element Modeling

As part of an effort to apply laser ultrasonics to stress evaluation, sequential thermal and mechanical finite element analyses were used to simulate heating a region of an aluminum surface by a laser pulse and the stress waves that result. As residual or applied stresses can be related to changes in wave velocities, time-of-flight measurements may be used to determine the stresses. One goal of the modeling effort was to improve time-of-flight measurements, and therefore resolution of the calculated stresses, perhaps by using calculated waveform shapes in model-based signal processing techniques [25]. Detailed finite element simulations of laser ultrasonics may also be used to aid development of techniques that can generate narrow band ultrasound. Because penetration of Rayleigh waves is frequency dependent, they can be used to obtain information about gradients near a surface. If the frequency of the laser generated Rayleigh waves can be controlled, laser ultrasound becomes a more useful tool for examining gradients in material properties or stresses at the surface of a part. Other aspects considered include simulation of stress gradient effects on waveforms, prediction of residual stresses in sample parts, and processing of measured velocity fields to extract stress component fields.

Material properties in most analyses were typical of most aluminum alloys. When plastic deformation was considered 6061-T6 properties were used

Waveforms

Computer programs for solving the thermoelastic equations describing wave generation and propagation caused by the interaction of a laser pulse with a metal surface have been developed over the last several years [26-28]. One approach is to manipulate the thermoelastic equations using transform techniques and then use numerical methods to invert the equations and solve for wave displacements. Another approach is to spatially discretize the geometry of the model using finite elements and integrate the equations of motion through time. The finite element formulation may be fully coupled or as a further approximation the thermal problem can be solved separately from the mechanical problem. The work reported here sought to develop a technique to use a general purpose finite element code (i.e. ABAQUS [29] or PRONTO3D [30]) to simulate surface waves generated in laser ultrasonics. A general purpose finite element code provides the advantages of large element and material libraries and the ability to consider complex geometries and boundary conditions. Sanderson's [28] computer code, which solves the coupled thermoelastic problem using numerical transform techniques, was used to validate the finite element model developed. Validation was performed using simple models and boundary conditions. Subsequent finite element simulations were used to examine the effects of simulated stress gradients (in-plane and through-thickness) on waveforms. The effects of temperature dependent properties and of including an elastic-plastic constitutive material model in the mechanical analysis were also briefly examined.

Finite element predictions of waveforms were generated using uncoupled thermal and mechanical analyses. A thermal analysis using a heat flux with Gaussian variations in time and space was used to simulate heating of an aluminum surface due to a laser pulse. The region modeled is large enough such that the boundaries away from the heat source do not change temperature during the time span of interest. This model is small in spatial extent compared to the mechanical model. Two types of finite element models were developed. Solid elements were used exclusively in one modeling technique, while the other used a combination of shell and solid elements. For the case of models constructed only of solid elements, the thermal and mechanical meshes are different, even in the regions where the two overlap, so the temperatures must be mapped from the mesh used in the thermal analysis to the mesh used in the mechanical analysis. Mechanical analyses were performed using explicit dynamic analysis codes [29,30]. For mechanical analyses with both shell and solid elements, thermal analyses were performed using only shell elements. For mechanical analyses combining shell and solid elements, there is a one-to-one correspondence of shell elements between thermal and mechanical models so mapping was not necessary. All analyses discussed here were 2D axisymmetric, but it is straightforward to extend the technique to 3D.

Figure 20 shows a schematic of the wave generation and propagation problem.

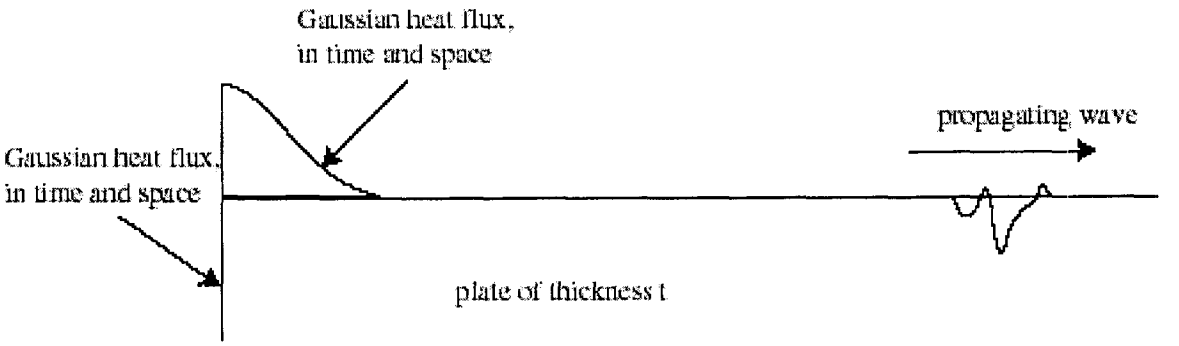

Figure 20. Schematic of surface wave generated by laser pulse.

Thermal Analyses

Thermal analysis procedures were first verified using analytically predicted temperature histories and distributions for a continuous wave laser heating a semi-infinite body [31]. A thermal analysis was performed using Coyote, a Sandia finite element code for multidimensional nonlinear heat conduction analyses [32]. The finite element mesh was constructed of four-node quadrilateral elements. A spatially Gaussian surface flux was used to model heat input by the laser. The finite element mesh for the 2D axisymmetric problem had many elements along the radius of the laser source in order to accurately capture the spatial variation in the laser source's energy deposition. Steady state and transient finite element results were nearly identical to calculations using the analytical model as shown in Figure 21.

Thermal analyses of a pulsed laser heating a surface of silver were then performed and the results compared with experimental data from [33]. In this experiment surface temperature changes due to the application of a 1068 nm laser with 1.8 mm diameter source spot size, 16 ns pulse duration, and 0.23 mJ energy deposition were measured. When reporting the data, an analytical solution was also presented for the temperature history at the center of the laser source. The model assumed a pulse uniform in space (radially) and triangular in time. Finite element simulations were performed using two laser pulse time histories. Both were Gaussian in space but one history was Gaussian in

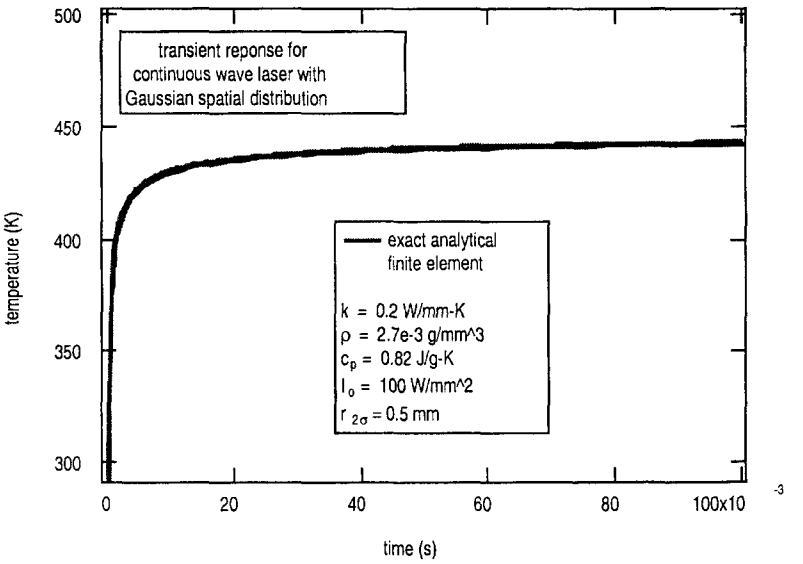

(a)

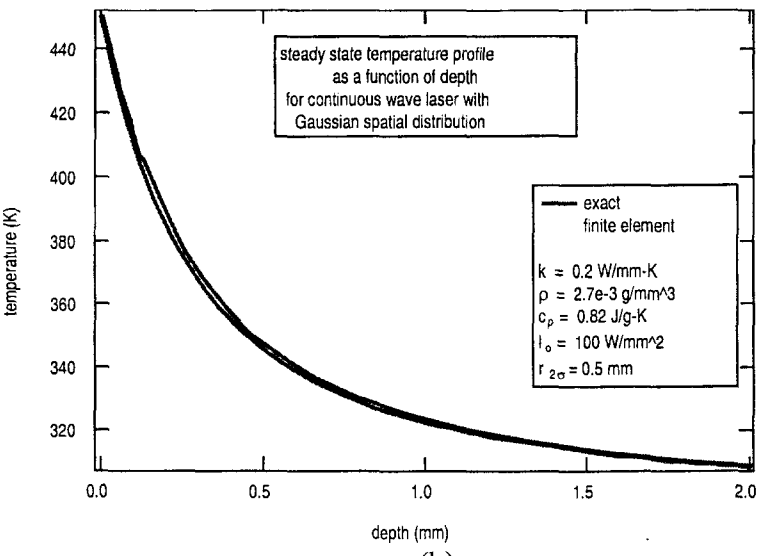

(b)

Figure 21. Transient at surface (a) and steady state through-thickness (b) thermal responses for aluminum plate heated by a continuous wave (CW) laser at center of disk. Comparison between analytical solution and finite element model results.

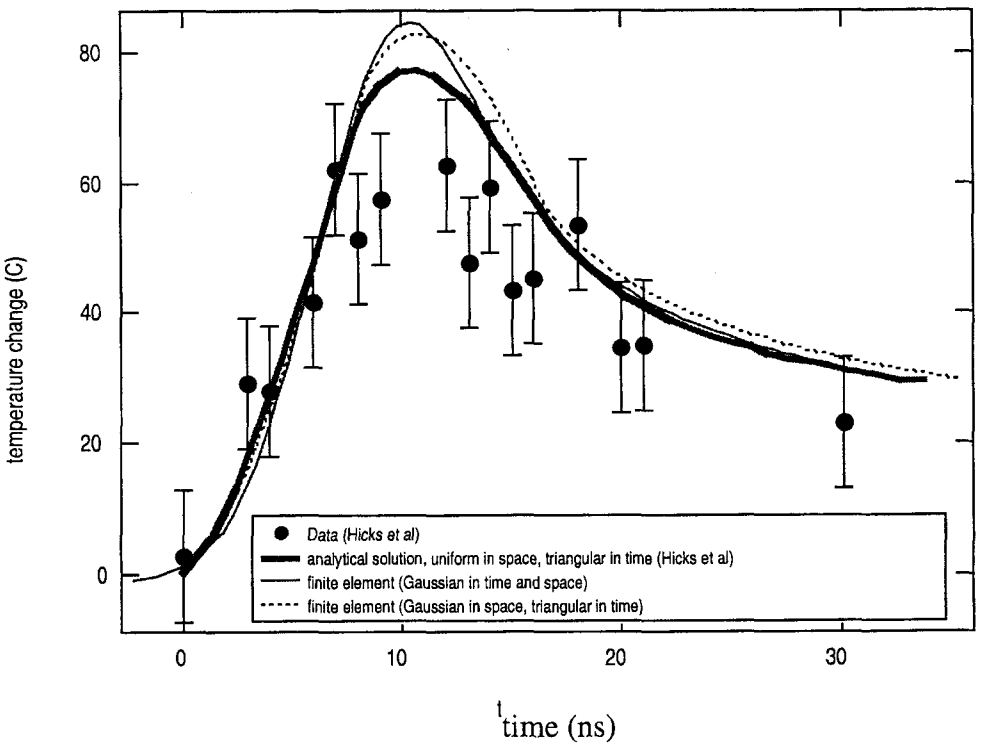

Figure 22. Comparison of thermal response caused by a laser pulse heating the surface of a silver plate. Comparison of finite element results with analytical results and experimental measurements.

time while the other history had a triangular pulse as a function of time. The finite element results compared quite well with the experimental and analytical results reported in [33] and are shown in Figure 22. The Gaussian pulse shape in time gives a peak temperature change approximately 10% higher than a pulse in which intensity does not vary with radius. The peak temperature change is slightly higher for the pulse Gaussian in time and space than for the pulse triangular in time and Gaussian in space.

When thermal analyses were performed using solid element models, very small elements were used near the surface in order to capture the thermal gradients early in time. Element dimensions were typically on the order of 10^{-4} mm near the surface in the region of the laser source. The domain of the meshes extended to 4 mm radially and 0.5 mm through the thickness. These distances were larger than the distance heat could diffuse in the maximum 6 microsecond duration of any of the analyses. The solid element models consisted of as many as 50,000 elements. Time steps were kept on the order of 0.1 ns during the duration of the pulse. Time steps were allowed to increase automatically after termination of the pulse. Thermal analyses were run to several ms to provide temperature histories for the full duration of the mechanical analyses.

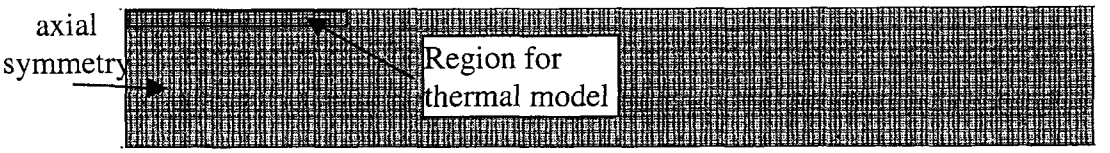

Figure 23. Mesh for mechanical finite element analyses constructed of continuum elements. The smaller domain modeled in thermal analysis is indicated by the boxed region in the top left of the figure. Thermal domain is 4 mm radially by 0.5 mm high. Mechanical analysis domain is 18 mm radially by 5 mm thick.

Mechanical Analyses

Most thermal analyses used temperature independent material properties. Energy fluxes were kept low enough so that melting and ablation would not occur, consistent with experimental observations. Results were transferred from the mesh used in the thermal analysis to a subset of the mechanical mesh using the Sandia utility code MERLIN [34]. Elements in the mechanical mesh that were outside the thermal model domain were kept at constant temperature during the duration of the mechanical analysis. Thermal and mechanical meshes were different, with elements in the thermal model being much smaller (as small as 10^{-4} mm) than those in the mechanical model ($\sim 10^{-1}$ mm) near the surface. The domain modeled in the thermal analysis was a subset of the mechanical analysis domain, as shown in Figure 23. Meshes for the mechanical analyses were typically meshed with uniformly sized square elements throughout the mesh. Element sizes were selected by requiring several elements over the wavelength of the highest frequency wave component thought to be important in the model. Typically, mechanical meshes consisted of uniformly sized square elements to avoid causing inadvertent reflections due to poorly shaped elements and regions of the mesh where elements do not smoothly transition in size. The uniform size and shape of the elements also reduces inadvertent filtering of waves that could occur when waves travel from finely to coarsely meshed regions. For a region 18 mm x 5 mm, 36,000 0.05 mm square elements were required. Although the finite element mesh used in the mechanical analyses was able to capture waves of relatively high frequency and had many elements within the laser source radius, it was too coarse to accurately capture the temperature gradient at the surface. In the thermal analysis, heat diffused to approximately 10^{-3} mm by 4 ns and approximately 0.07 mm by 6 microseconds in 2024 aluminum for a 4 ns duration, 2.25 mm diameter pulse. In the mechanical mesh just described, the temperature gradient is spread over only one element during the time of wave generation (about the time required for a longitudinal wave to traverse the laser-heated surface). To better capture the thermal gradient but still keep the model size relatively small, the temperatures from the thermal analyses were applied to a layer of shell elements which were attached to a solid element model of the plate. Figure 24 shows an example of this arrangement.

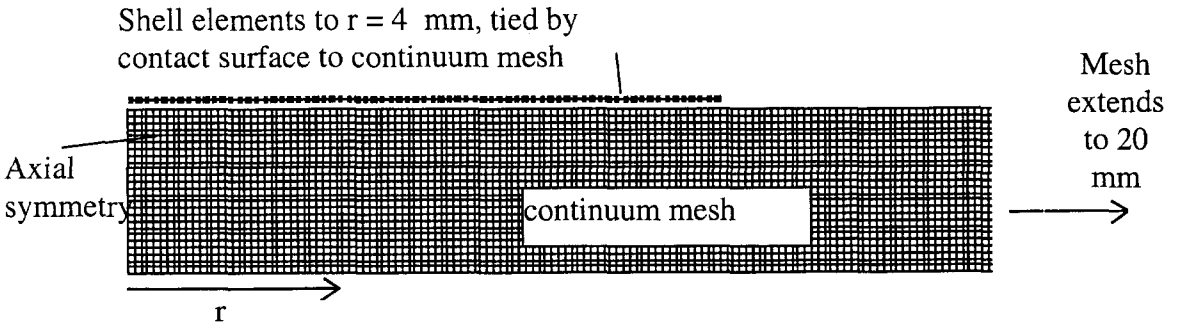

Figure 24. Finite element mesh combining shell elements and continuum elements.

The finite element code ABAQUS [29] was used to experiment with the shell/solid element model. Shell elements were tied to the base structure using contact surfaces, while the base structure was discretized using solid elements. The user may specify temperatures at a number of equally spaced points through the thickness at each node of the shell element. Heat transfer as well as thermal stress analysis problems may be modeled this way, with temperature histories from the thermal analysis used as the loading in the mechanical analyses. Thermal analyses required much less computer time when shell models were used than solid element models of the same domain. In addition, no mapping of the temperatures between different thermal and mechanical meshes was required.

When shell elements were used, meshes were constructed of 2-node linear axisymmetric shell elements (ABAQUS type SAX1) and square axisymmetric 4-node bilinear quadrilateral elements with reduced integration (ABAQUS type CAX4R). Shell elements were at the same location and had the same thickness as in the thermal analysis. Shell elements with 19 integration points through the thickness were used. Solid element nodes coincident with shell element nodes were constrained to follow them through use of the TIED contact constraint in ABAQUS. In both thermal and mechanical analyses presented here, shell element meshes only extended to a radius of 4 mm, which was larger than all laser spot radii considered. Mechanical meshes extended to 20 mm to avoid reflections from the edge of the model during the period of interest. ABAQUS also has an infinite element for modeling non-reflective boundaries that could be used to reduce the mesh size. Out of plane displacements were recorded 8 mm from the center of laser heating. Figure 24 shows a schematic of the mesh.

Element sizes of 0.1, 0.05, and 0.025 mm (associated with coarse, medium, and fine meshes, respectively) were used. These dimensions were selected because they are able to capture Rayleigh waves of frequencies 3, 6, and 12 MHz respectively, assuming adequate resolution at 10 elements per wavelength and assuming a Rayleigh wave speed in aluminum of 3 mm/ms. Mechanical properties used were Young's modulus = 69 GPa, Poisson's ratio = 0.327, and density of 2.77×10^{-3} g/mm^{-3}.

Results

Figure 25 shows a comparison of finite element results with transform technique results from Sanderson [28] for 4 mm and 2.25 mm diameter spot sizes, 4 ns pulse duration, and 5 mm thick aluminum plate. Due to the similarity in waveforms for the medium and fine meshes, only the coarse and fine mesh results are shown. For both excitation diameters the coarse mesh under predicts the peak associated with the Rayleigh wave arrival (~2.7 ms) and the peak near 3.1 ms. The peak near 3.1 ms occurs

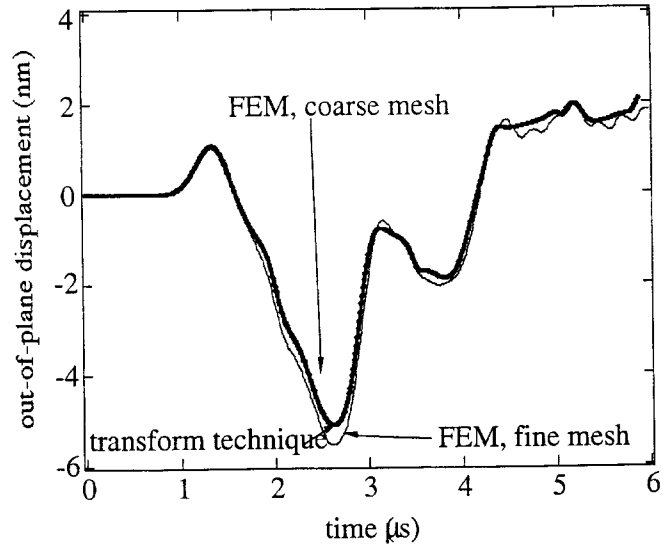

(a)

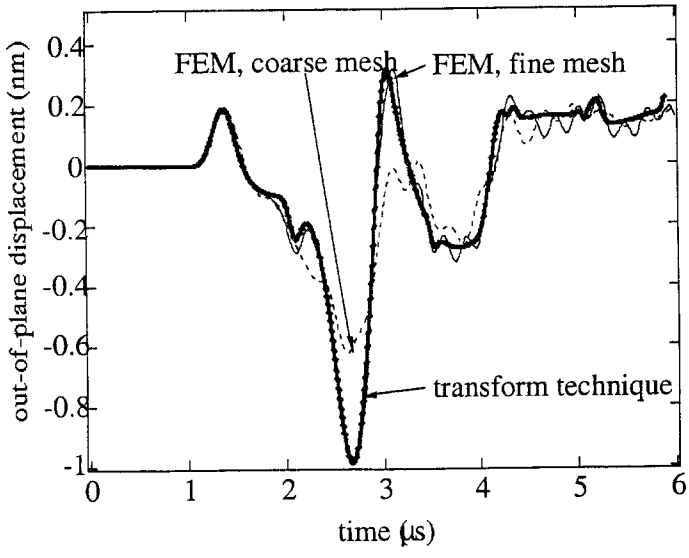

(b)

Figure 25. Comparison of computed surface displacements from finite element simulations for three mesh densities with results from transform solution. (a) Laser spot diameter of 4 mm, (b) spot diameter of 2.25 mm. Both plots are for 4 ns pulse duration and 5 mm thick aluminum plate. Measurement location was 8 mm from center of laser heat source.

between the arrival of the Rayleigh wave from the epicenter and the arrival of the SV wave from the laser source far edge. Fine mesh magnitudes are slightly larger than those from the medium mesh. There is reasonably good agreement between the transform technique solution and the medium and fine finite element meshes. In Figure 25b, the fine-mesh finite element method (FEM) solution slightly overshoots the dip occurring near 2 ms, which is around the time the reflected P wave and the Rayleigh wave from the source near edge arrive. The peak near 3.1 ms arrives slightly late in the FEM waveform, and there is some oscillation in the FEM results after about 3 ms. Stiffness proportional damping was specified to minimize relatively high frequency ringing (> 10 MHz) in the waveforms. The amount of damping added was typically on the order of 0.75 ns and was kept to the minimum required to prevent spurious oscillations as the addition of damping reduces the time step used in the analysis. Figure 26 shows an example of the effect of stiffness proportional damping for a 5 mm thick aluminum plate, 9 mm away from the laser source center. The stable time step without damping for these analyses was 3.2 ms. The addition of damping can significantly reduce the time step used and therefore increase run time, as discussed in the ABAQUS/Explicit user manual [29]. It was observed that the frequency of oscillation increased as mesh size decreased. Also, the duration in time decreases as the frequency increases. This may be a Gibb's-like [35] phenomenon in which case the oscillation could not be removed without damping, regardless of the fineness of the mesh, but the extent in time could be minimized by using a fine mesh.

Although agreement between finite element and integral transform results are good in a general sense and was adequate for purposes considered here, better agreement over the entire time of interest should be attainable. The temporal distributions of the heat flux are slightly different between the transform technique and finite element models, but those differences are not expected to significantly alter the waveforms. The shell/solid models are quite efficient but the "best" agreement with transform method results probably are obtainable through all-solid models. With the shell/solid technique there were always some issues with the shell/solid interface that could not be completely resolved.

Spicer, like Sanderson [28], formulated fully coupled equations of classical and temperature rate dependent thermoelasticity. The laser source was represented by an equivalent elastic boundary source to predict displacements in infinite isotropic plates of finite thickness. Displacements were calculated using Laplace-Hankel transform solutions inverted numerically. The curves representing Spicer's calculations were digitized from figures in the literature and so are somewhat less smooth than the curves he reported.

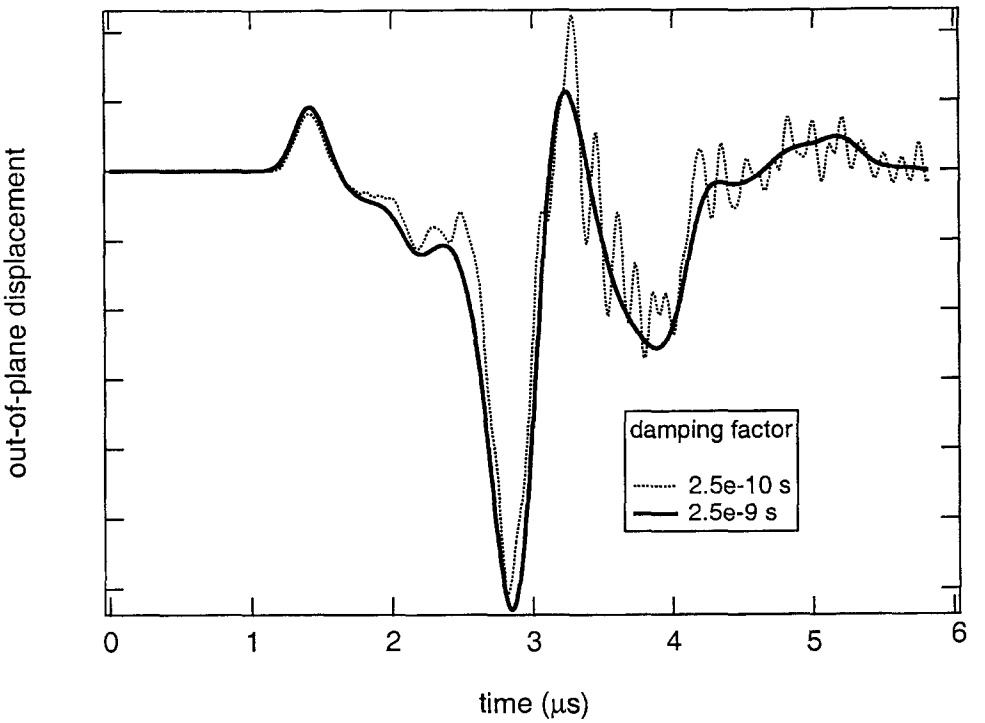

Figure 26. Sample waveforms generated using ABAQUS/Explicit showing the effect of stiffness proportional damping on preventing spurious oscillations.

Figure 27 shows comparisons between the finite element results and Spicer's [26] integral transform results for a 1.125 mm radius, 4 ns duration, 0.2 mJ pulse recorded 9 mm from the source center. Material properties were Young's modulus = 70 GPa, Poisson's ratio = .3, and coefficient of linear thermal expansion = 23e-6 C^{-1}. As the analysis was elastic and temperature independent properties were used in both thermal and mechanical analyses, displacements from the mechanical analyses were scaled to match peak displacements from Spicer's data.

The features displayed in Spicer's data, which agreed very well with his experimental measurements, are also exhibited in the finite element displacement curves. In order to remove numerical oscillations in the finite element displacement histories, a small amount of stiffness proportional damping was used. For the mesh with 0.05 mm square elements, time steps in the mechanical analyses were on the order of 5 ns. It was observed that a stiffness proportional material damping factor (which has units of time) of 0.75 ns removed most of the spurious oscillations from the displacement histories in the ABAQUS analyses. If a value an order of magnitude less than this is used, "spurious" oscillations begin to appear in the waveforms as shown in Figure 26. Comparisons of the waveforms between finite element and transform technique solutions show the finite element curves are somewhat smoother than the semi-analytical curves. Addition of stiffness proportional damping does remove the unwanted numerical oscillations, but it

also tends to smear many of the features, particularly those of short duration and relatively large magnitude.

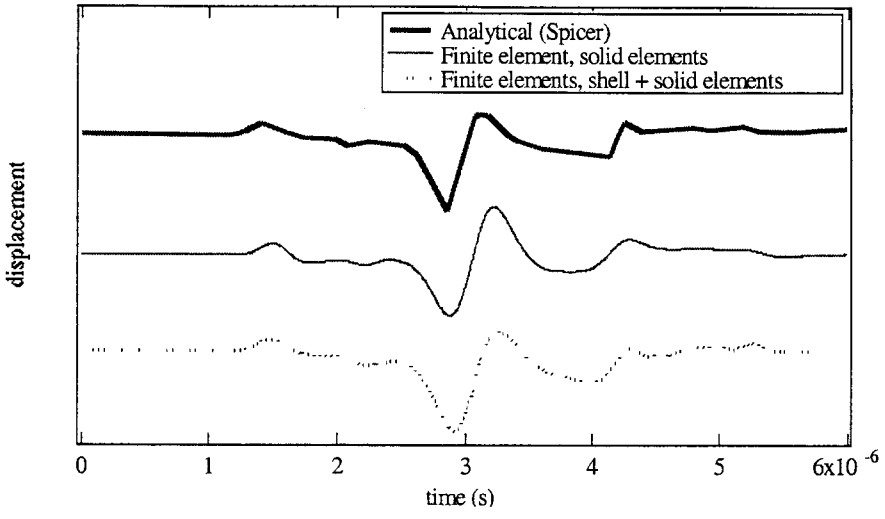

Figure 27. Comparison of surface waveforms from Spicer's [26] integral transform solutions, all continuum element finite element model, and shell and continuum finite element model for 1.125 mm radius laser source, 4 ns pulse duration, 0.2 mJ pulse on aluminum. Measurement location is 9 mm from center of excitation. Displacement units are not shown but peak-to-peak values are on the order of 0.2 nm/mJ of deposited energy.

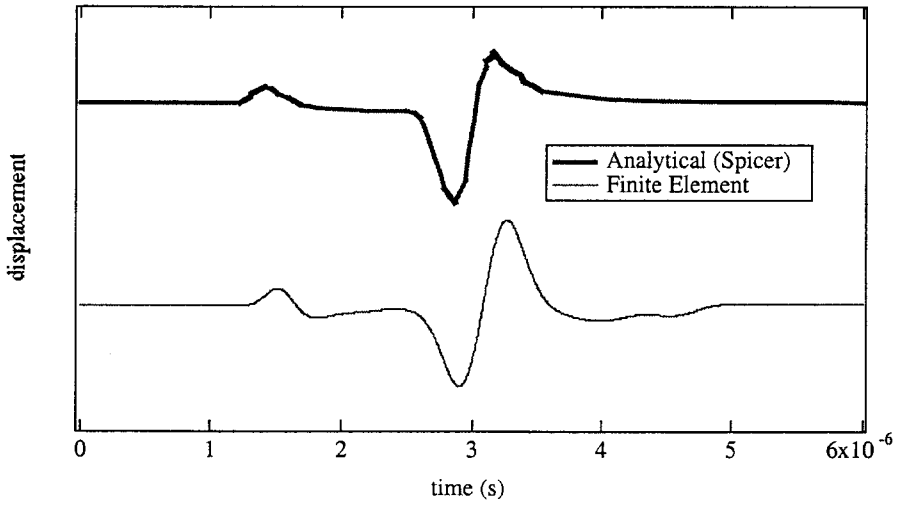

Figure 28. Comparison of surface waveforms as calculated by Spicer [26] and a continuum element finite element model. Waveforms are for point on same surface as laser source, 9 mm from source center for 25 mm thick aluminum plate for a 2.25 mm diameter laser source. Peak-to-peak displacements are on the order of 0.12 nm/mJ of deposited energy.

The surface waveforms do not appear to be particularly sensitive to the steepness of the temperature gradient in the material under the laser source. The meshes used to generate the results in Figures 27 and 28 used 0.05 mm square elements. This is quite large compared to the depth of heat penetration during the first 100 ns which is approximately 7 μm. The temperature gradient in the mechanical analyses was much smaller than in the thermal analyses due to the difference in element sizes at the surface. The shell+solid model results shown in Figure 27 were generated using 0.01 mm thick shell elements with 15 temperature points through the thickness, providing a much larger thermal gradient than the solid element models. The shell/solid waveform is in somewhat better agreement with Spicer's [26] results than the solid model waveform.

Stress Gradients

Once the waveforms for the case of temperature independent material properties, elastic mechanical response, and stress-free structure were determined to agree reasonably well, the finite element models were modified to briefly consider situations difficult if not impossible to solve with transform techniques. Figures 29a and 29b show how waveforms change in the presence of simulated through-thickness and in-plane stress gradients, respectively. These waveforms were generated using the coarse (0.1 mm) finite element mesh to demonstrate the trends that might be expected. For the through-thickness case, stress gradients were simulated by varying Young's modulus in a way such that the wave speed varied linearly from its baseline value at the surface to a value of 10% or 20% greater at the bottom of the plate's 5 mm thickness. Similarly, the in-plane stress gradient case is simulated by modifying Young's modulus such that the wave speed varies linearly from its baseline value at r=0 to a value 10% or 20% greater at the monitored location r=8 mm. It is recognized that this method of simulating stress gradients is not totally correct but the general trends in the waveforms should be representative. The stress gradients can be reproduced more correctly, for instance in the through-thickness stress gradient model, by using relations developed by Man [36]. The stressed plate could be modeled by layers of orthotropic material with elastic constants modified by the amount of stress in each layer.

Figure 29a shows that as the magnitude of the stress gradient (wave speed) increases, from its reference value at the surface to a greater value at the plate bottom the longitudinal arrival time (around 1.2 ms) does not change significantly. This is because this wave is confined to the surface layer which has the baseline wave speed. However the Rayleigh wave arrival near 2.7 ms is reduced in magnitude and arrives sooner. Reflected waves which have traveled through the plate thickness also arrive sooner. The largest positive peak near 3 ms arrives earlier but does not undergo quite the same trend in magnitude change as the Rayleigh waves. Features of the waveform near 4 ms on the baseline curve have a fairly uniform shift in time and a still different trend in change in magnitude. For comparison, a waveform generated using an elastic modulus that gives a 20% higher wave speed throughout the body is also shown. Arrival times are uniformly 20% higher than that of the baseline case (no gradient), as expected, and no significant change in peak magnitudes is observed. Figure 29b shows that for the case of an in-plane

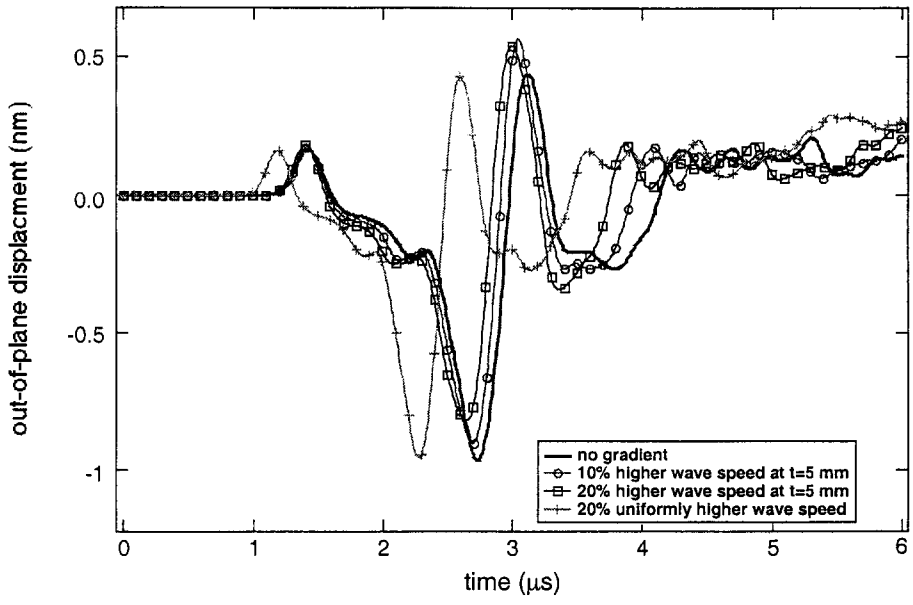

(a)

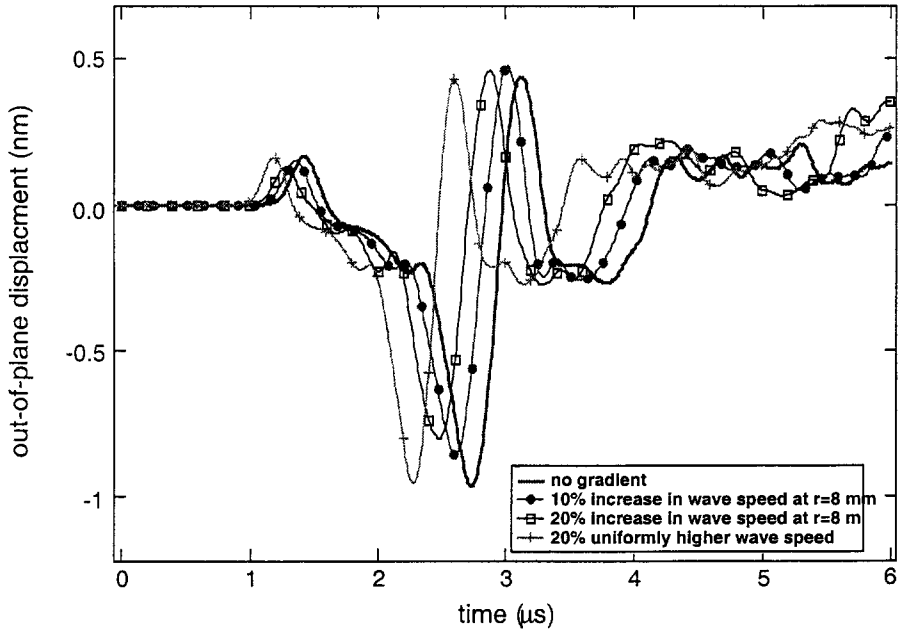

(b)

Figure 29. Effects of through-thickness (a), and in-plane stress gradients (b) simulated by varying Young's modulus. For the through-thickness gradient simulation, the 10% and 20% numbers reflect the increase in wave speed at the bottom of the plate relative to the wave speed at the top surface. For the in-plane gradient simulation, the wave speed is 10% and 20% faster at r=8mm than it is at r=0 mm. Laser source parameters were r=1.125 mm, duration = 4 ns, energy = 0.2 mJ. Results are for 5 mm thick 6061-T6 aluminum plate.

stress gradient, the P wave arrival times decrease as the simulated stress gradient is increased. The magnitudes of the P-waves (~1.2 ms) can be seen to be decreasing somewhat as the gradient is increased. Rayleigh waves, which travel along the free surface and whose penetration is frequency dependent, will experience the same increase in phase velocity at all frequencies because the in-plane stress gradient is uniform through the thickness. This is in contrast to the through-thickness gradient case (a), where Rayleigh waves with longer wavelengths will travel faster than those with shorter wavelengths since the wave speed is higher at the bottom of the plate.

Although the method for simulating the gradients is only approximate, the trends in waveforms are expected to be representative. More detailed explanations of the observed trends should be possible by studying the frequency and phase content of the waveforms.

The Effect of Temperature Dependent Properties and Mechanical Constitutive Model on Waveforms

A brief study was performed to examine the effect of using temperature dependent thermal and elastic material properties and to observe the effect of including plasticity in the mechanical model. Several combinations of temperature dependence in the thermal and mechanical analyses along with the inclusion of plasticity were considered, with the results shown in Figure 30. In order for temperature dependence to play a more significant role, the energy of the laser pulse was increased from 0.2 mJ to 0.6 mJ. This caused the highest temperature reached for the r=1.125 mm, 4 ns duration pulse to be close to the liquidus temperature for 6061-T6 aluminum (around 925 K) when temperature dependent properties were used, and near 1360 K when temperature independent thermal properties were used. A bilinear elastic plastic constitutive model was used with a yield stress of 330 MPa at room temperature decreasing to approximately zero at the liquidus temperature. Forces due to ablation were not considered.

Figure 30 shows the results, along with a table showing the status of thermal and mechanical temperature dependence and if plasticity was considered. Using temperature dependent elastic and thermal properties significantly decreased the peak magnitudes in the waveform. The shape of the waveform was more effected by including plasticity than by temperature dependent material properties.

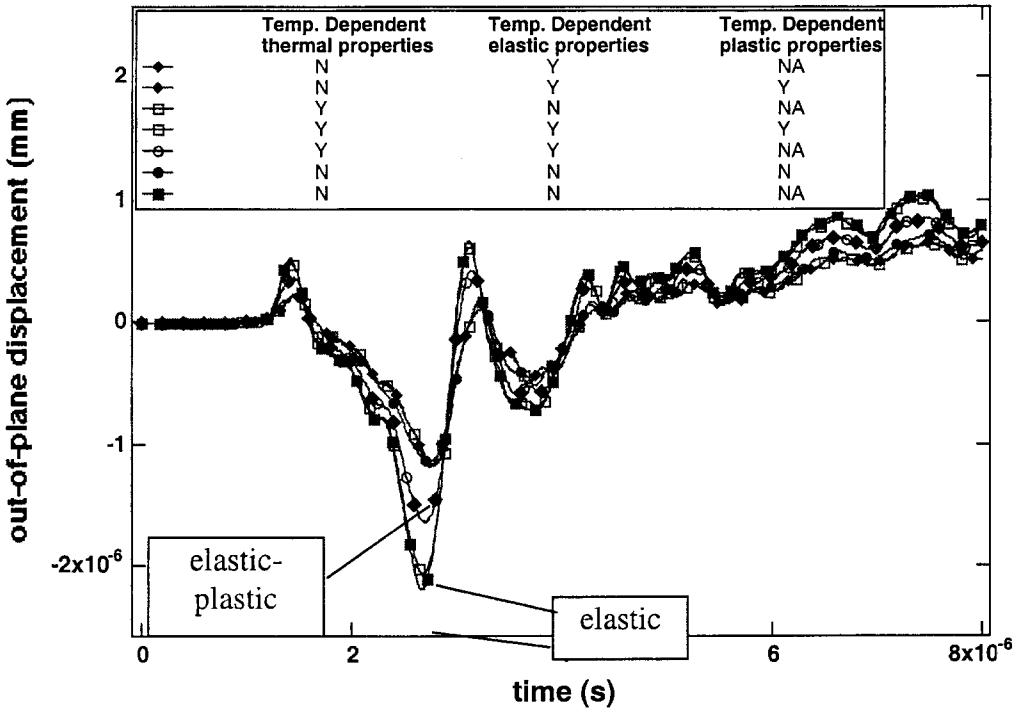

Figure 30. Finite element model waveforms showing effect of temperature dependent material properties and use of bilinear mechanical constitutive model. NA = not applicable.

Frequency Content as a Function of Laser Spot Diameter

Figure 31 shows how the frequency content of a signal changes as the diameter of the laser source is changed. The data for these curves comes from waveforms generated using Sanderson's [28] integral transform solutions. Pulse duration, within the capabilities of the Q-switched laser system we were using (say durations between 2 ns and 20 ns), have almost no effect on the waveform's shape or frequency content. However, as shown in Figure 31, the smaller the spot diameter the greater the frequency content of the signal.

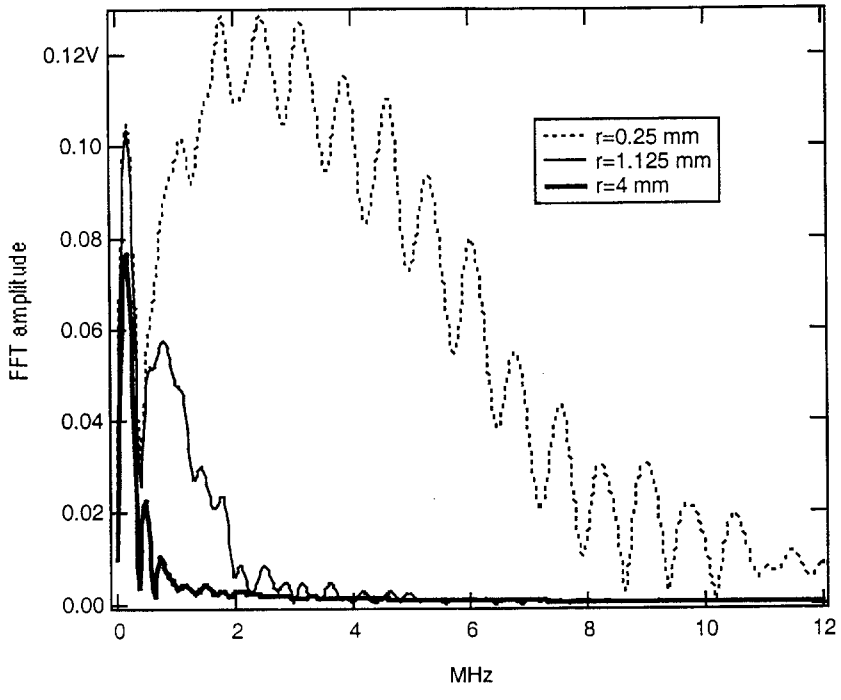

Figure 31. Fast Fourier transforms of surface waves for different laser source diameters showing frequency content of signal increasing as source diameter decreases. Results are for 4 ns duration, 0.2 mJ pulse on 5 mm thick aluminum plate.

Narrow Band Generation

There are two approaches to using laser ultrasonics for measuring through-thickness material property and stress gradients. One is to make use of the broadband nature of the generated surface wave and process it to extract information regarding the velocity at which component waves of different frequencies travel. Because Rayleigh waves penetrate approximately one to two wavelengths into the material, long wavelength (low frequency) waves sample material through a greater thickness of the part than do short wavelength (high frequency) waves. For a stress free homogeneous material Rayleigh waves are non-dispersive, that is all frequency components of the surface wave travel at the same speed. When material properties or stress varies through the part thickness, different frequencies travel at different speeds. Therefore if the

material is known to be homogeneous but the wave speed varies with depth, a stress gradient can be measured by obtaining the phase velocity as a function of frequency.

The second technique is to try to control the frequency content of the laser ultrasonic wave. There are two ways to do this, temporal modulation and spatial modulation. Temporal modulation involves varying the amplitude of a long laser pulse so that a significant fraction of the ultrasonic energy is focused into a band centered around the modulation frequency. Spatial modulation typically involves multiple excitation location spots, with the energy distributed using multiple fiber optic lines or by splitting a single beam using a diffraction grating. Both spatial and temporal modulation have the effect of causing a pulse train to arrive at the detection location, with the spacing of the pulses in the train determining the frequency of the train. Two advantages of narrow band waves is that narrowband receivers such as EMATs can be used and the signal to noise ratio is improved because it is inversely proportional to the system bandwidth.

To help aid experimental evaluation of these approaches, narrow band generation by spatial modulation was simulated. The method involved generating a characteristic pulse for a given laser excitation spot diameter and pulse duration, then superposing this solution based on the number and spacing of sources being considered. Figure 32 shows a schematic of four laser sources separated by a distance d. The receiver's location is also indicated. If all of the sources receive the same laser pulse at the same time, either through multiple fiber optic lines or splitting a single source beam using a diffraction grating, under certain conditions a pulse train will be generated.

Figure 33 shows an example of the surface wave observed 8 mm from the closest source for a laser spot diameter of 0.5 mm and various numbers of sources and spacing. Pulse trains are shown for source spacing of 0.6 mm and 3.6 mm. For the 0.6 mm spacing, results are shown for 2, 4, and 8 excitation spots. Figure 33 shows the number of pulses in each corresponding train to be the same as the number of excitation spots. Figure 34 shows the FFT's of these signals, showing how the signal center frequency of 5 MHz becomes increasingly well defined as the number of source spots is increased. When the spacing of the pulses (and sources) is increased as for the 3.6 mm spaced sources, the signal energy is shifted into periodically recurring bands above the modulation frequency of 1 MHz.

Figure 34 indicates that for these particular pulse parameters, at least 4 sources are needed to significantly increase the narrow-bandedness of the signal. Similar analyses can be performed using different spot sizes and pulse profiles to determine optimum source spacing for each.

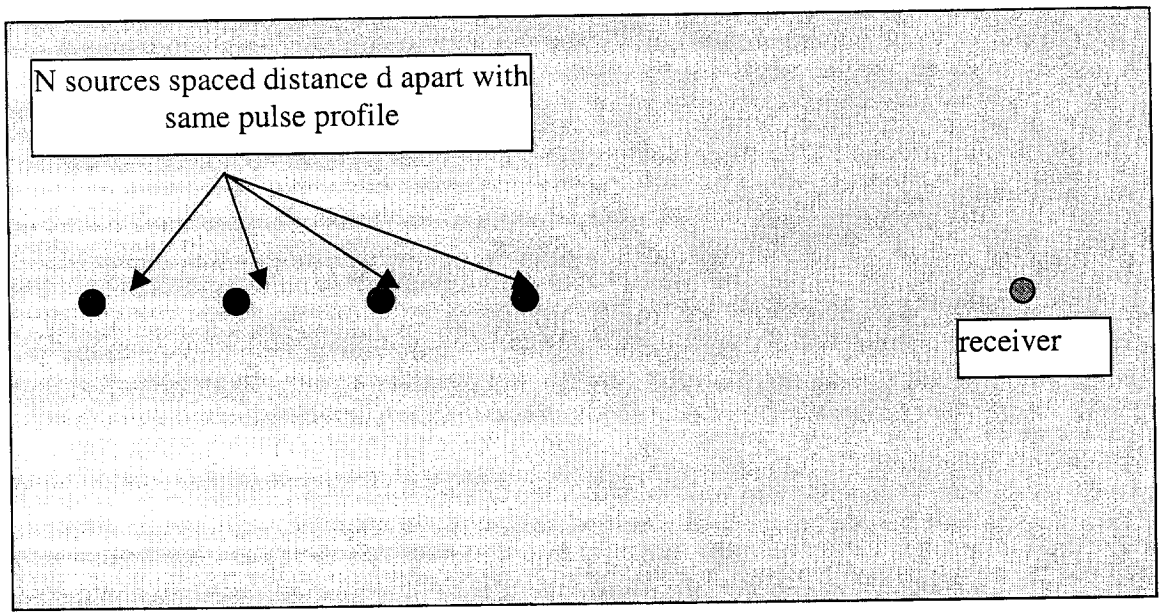

Figure 32. Schematic for spatially modulating a laser pulse to generate narrow band ultrasonic waves. Laser excites the four (N) sources at the same time with the same pulse profile. Because of the differences in travel distance to the receiver, a pulse train as in Figure 33 is observed at the receiver.

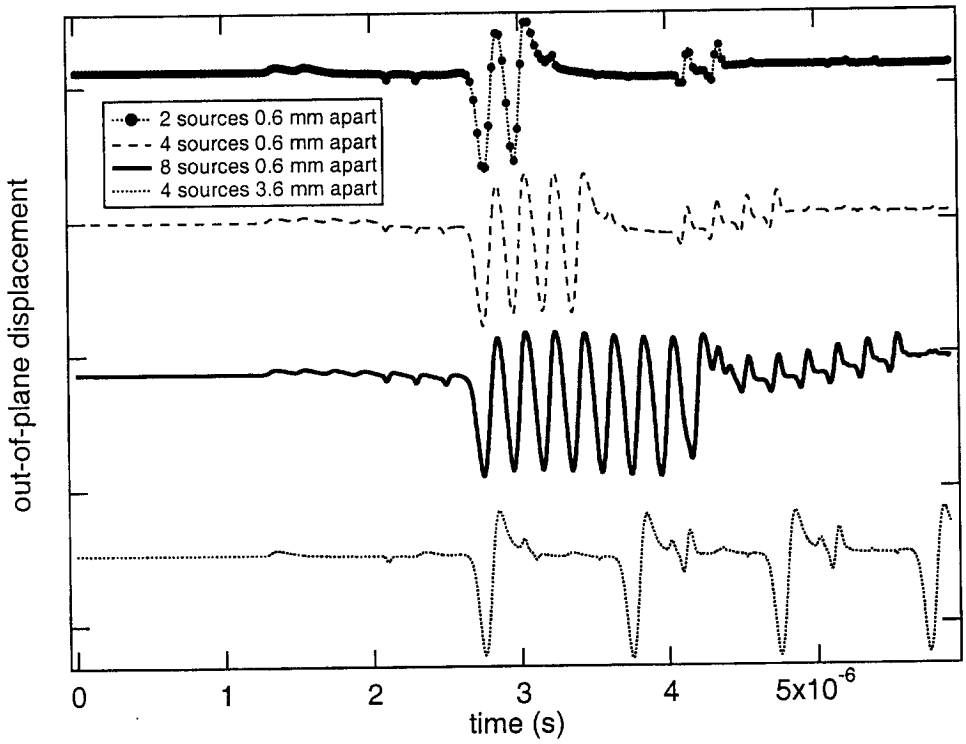

Figure 33. Pulse trains at receiver 8 mm from closest laser source for laser source 0.5 mm diameter, 4 ns duration, and 0.2 mJ energy for 5 mm thick aluminum.

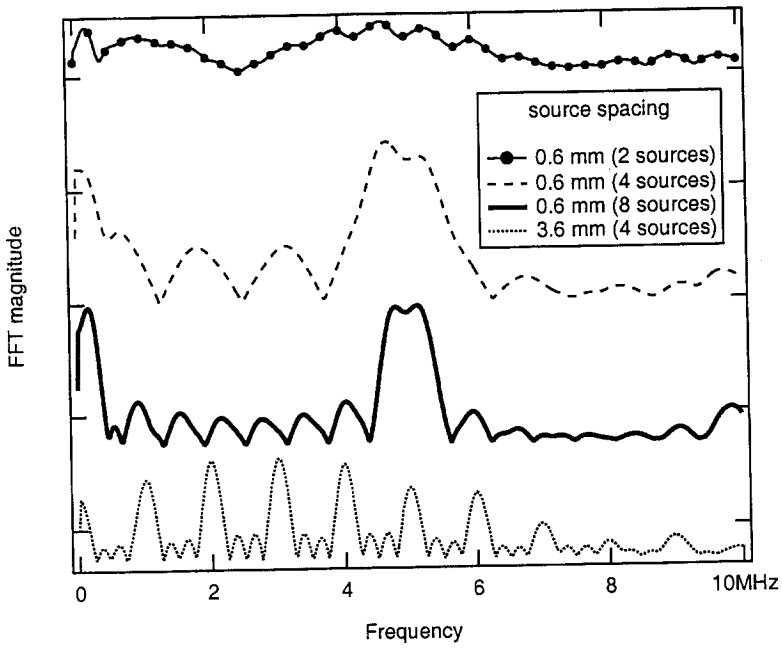

Figure 34. Frequency content of pulse trains shown in Figure 13. Note how increasing the number of sources with source spacing fixed narrows the bandwidth of the received pulse (top 3 curves). A pulse train of discrete pulses distributes the energy in periodically recurring frequencies both above and below the modulation frequency (1 MHz).

Evaluating Stress Components from Relative Velocity Measurements

Rayleigh waves have different acoustoelastic constants normal to and parallel to the direction of loading (K_{11} and K_{12}). The sums and differences in normal stresses may be related to the relative velocities by the following expression,

$$\sigma_{11}-\sigma_{22} = \left(\frac{\Delta V_1}{V_o} - \frac{\Delta V_2}{V_o}\right) A$$

$$\sigma_{11}+\sigma_{22} = \left(\frac{\Delta V_1}{V_o} + \frac{\Delta V_2}{V_o}\right) B$$

$$A = \frac{\mu\,\delta_o}{K_{11}-K_{12}};\quad B = \frac{\mu\delta_o}{K_{11}+K_{12}};\quad \delta_o = \frac{C_{R_o}}{C_{S_o}}, \qquad (10)$$

where m is the shear modulus, C_{R_o} and C_{S_o} are the Rayleigh and shear wave speeds in the unstressed material, respectively. If the reference state is known, σ_{11} and σ_{22} may be solved for, after which σ_{12} may be determined using the equations of equilibrium. If the reference state is not known, the procedure changes. For example, if $K=K_{11}=K_{12}$, we would have

$$\frac{\Delta V}{V_o} = K\,(\sigma_{11}+\sigma_{22})$$

A Poisson's equation for the shear stress in terms of $\sigma_{\alpha\alpha}$, (a=1,2) can be derived. This equation along with values of the shear stress on the boundary provide σ_{12}. The equations of equilibrium can then be used to obtain σ_{11} and σ_{22}. If K_{11} is unequal to K_{12}, this approach can be used in an iterative manner. This technique has been applied by Dike and Johnson [37,38]. The method is not demonstrated here because a full-field mapping of velocity change due to stress is required. Full-field measurements of velocity changes have not yet been measured using our LU technique.

Structural Analyses for Validation Purposes

Two specimen geometries were selected to use for residual stress measurements as described in the Stress Measurement section of this report. One was a 0.5 in thick 6061-T6 aluminum ring approximately 6 in outside diameter and 3.6 in inside diameter, loaded diametrally to a displacement of 0.39 in and then unloaded. The other specimen was a 6061-T6 aluminum pipe, approximately 1.5 in outside diameter, 8 in long, and 0.1 in wall thickness subjected to an autogenous (no filler wire) gas tungsten arc weld. The ring was selected because it had been used to validate the residual stress evaluation technique using longitudinal waves [37, 38]. The welded pipe was selected as a validation specimen due to its similarity to pipes used in gas bottle weld development work. Stainless steel 304L was used for that work, but due to aluminum's larger acoustoelastic constant (about 4 times larger than steel's), aluminum was used for the current validation effort.

Finite element analyses were performed simulating the deformation of the aluminum ring and the pipe. Figure 35 shows the x-component of residual stress in the ring after compressing 1 cm and releasing. Figure 36 shows the residual axial stresses in a 304 L stainless steel pipe subjected to an autogenous GTA girth weld. Figures 37a and 37b show the expected relative velocity fields for the deformed aluminum ring. The figures were constructed by taking the finite element model results and applying equations (1) and (2). This sort of analysis not only provides residual stress fields for comparing with experimentally determined stresses, but also provides guidance as to where measurements may be expected to be of the best quality.

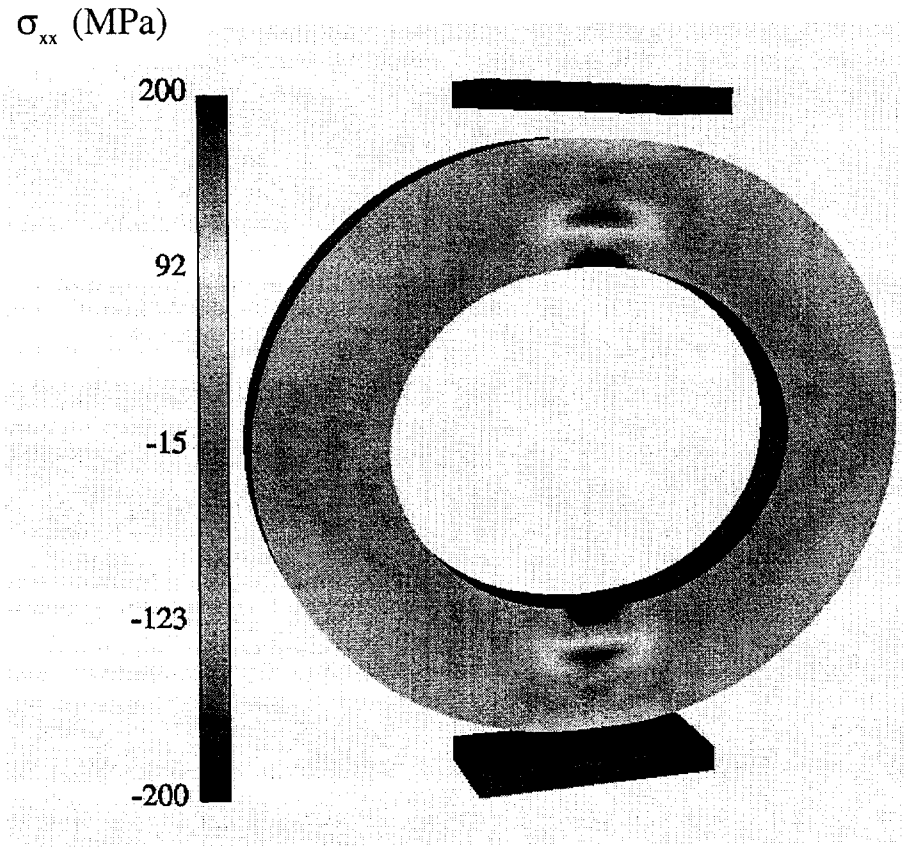

Figure 35. Predicted x-component (horizontal) of residual stress in diametrically compressed 6061-T6 aluminum alloy ring.

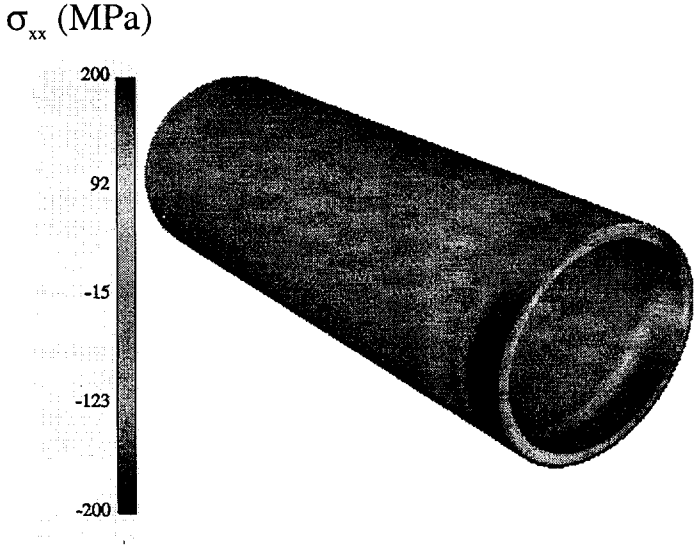

Figure 36. Predicted axial stress in stainless steel 304 L pipe after autogenous gas tungsten arc girth weld. Only half of model is shown, near end of pipe has axial symmetry condition specified.

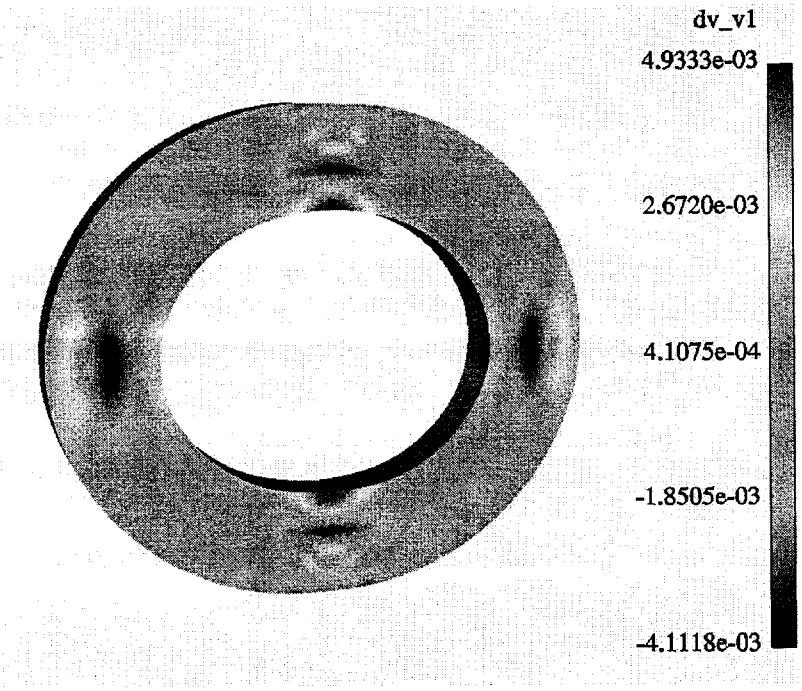

(a)

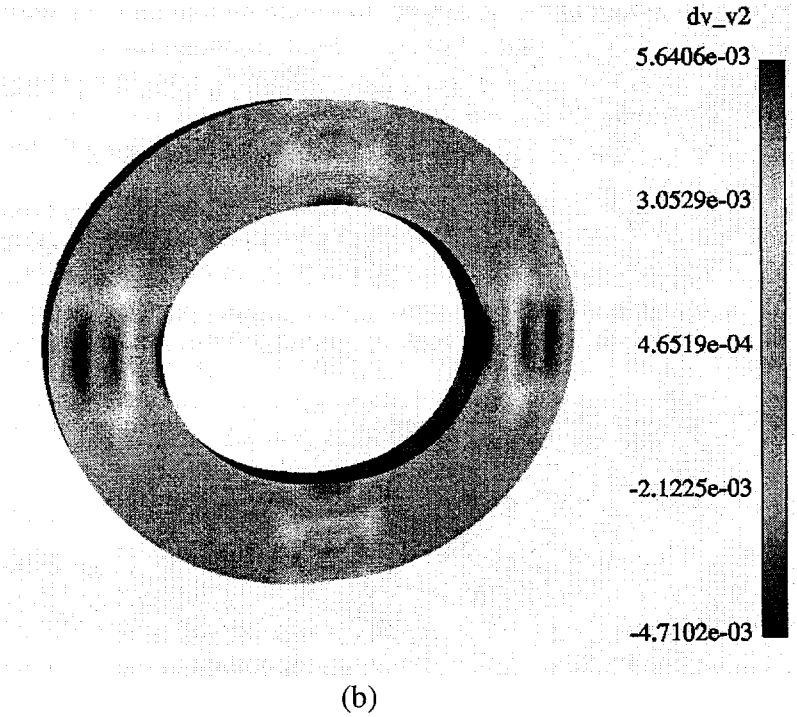

(b)

Figure 37. Predicted relative velocity change for aluminum alloy 6061-T6 with residual stresses for (a) x- (horizontal) direction, and (b) y- (vertical) direction. Acoustoelastic constants used were K_{11}=-0.022 / GPa and K_{12}=0.0095 / GPa.

Residual Stress Evaluation

The goal of this research is to investigate the applicability of LU in stress evaluation. After developing LU techniques and obtaining the acoustoelastic behavior of AA6061, experiments were performed to apply this approach to some simple structural members.

Diametrically Compressed Ring

A ring made of AA6061-T6 had the following dimensions: outside diameter D_o = 6", inside diameter D_o = 3.6", and thickness t = 0.5". The ring was compressed diametrically in the y- (or 90°) direction about 0.4" on an Instron System and unloaded. The load-displacement curve is shown in Figure 38, and the deformed ring is displayed in Figure 39. The circular ring became oval. Clearly, part of the ring was plastically deformed, and residual stresses were developed. The finite element simulated load-displacement curve is also shown in Figure 38. The difference at the initial part of the loading is due to the misalignment of the ring in the loading frame. We observed that the plastic deformation, where the platens contacted the specimen, was not symmetric.

From finite element analysis, predicted relative velocity fields are shown in Figure 37. The largest variation in velocity field is along the x- and y-directions (or 0° and 90°) with Rayleigh waves propagating in the y- and x-direction, respectively. Our LU measurements were based on this observation. The deformed ring was mounted on a stage, which allowed the ring to travel horizontally. For 0° measurements, the ring's x-axis was aligned horizontally and y-axis was aligned vertically. Two receiving spots illuminated by the CW laser were aligned vertically and were 12 mm apart, approximately at y = ± 6 mm, as shown in Figure 40. We horizontally scanned TOF of vertically traveled ultrasonic waves to obtain $\Delta V_y/V_y^\circ|_{y=0}$. The ring was then rotated 90 degrees for a measurement of $\Delta V_x/V_x^\circ|_{x=0}$.

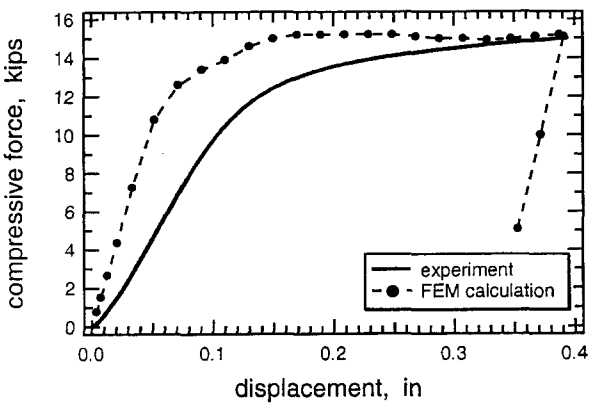

Figure 38. Load-displacement curve of the AA6061-T6 ring subjected to diametrical compression.

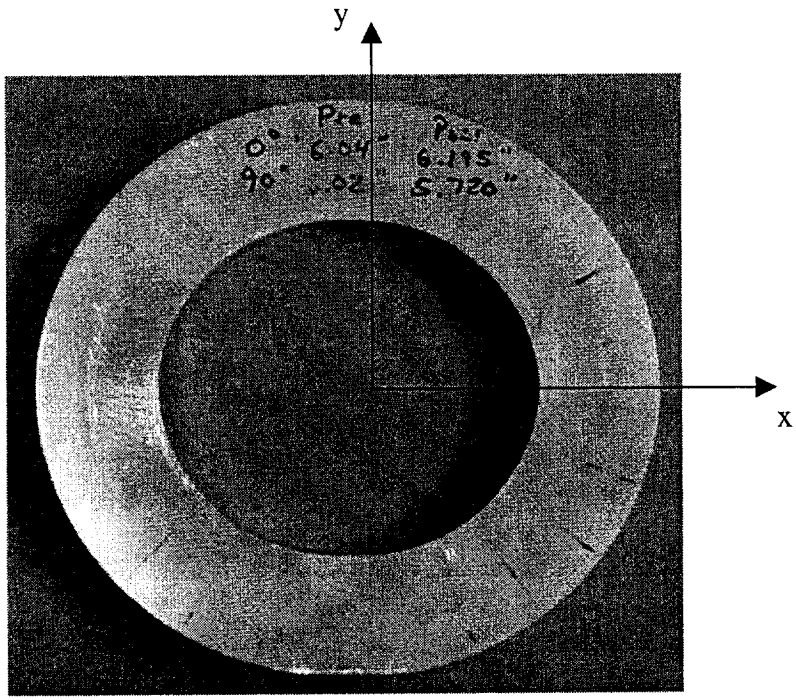

Figure 39. The deformed ring.

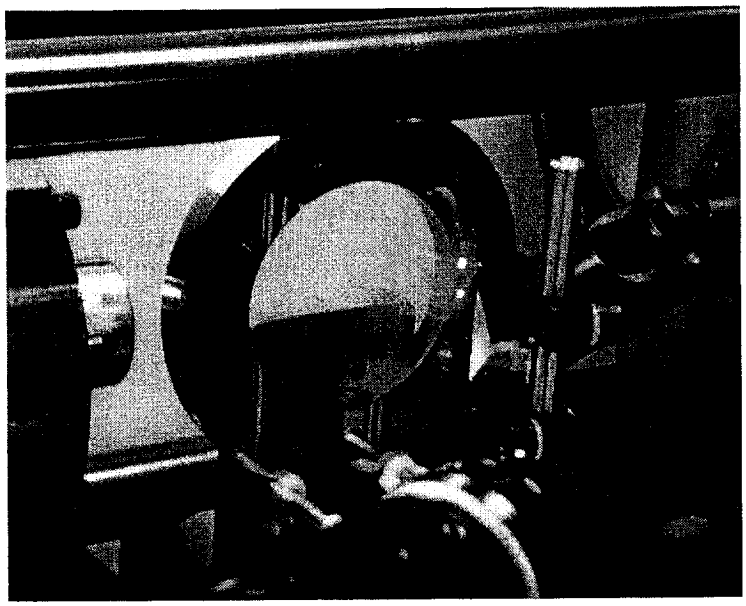

Figure 40. TOF measurement on a compressed ring.

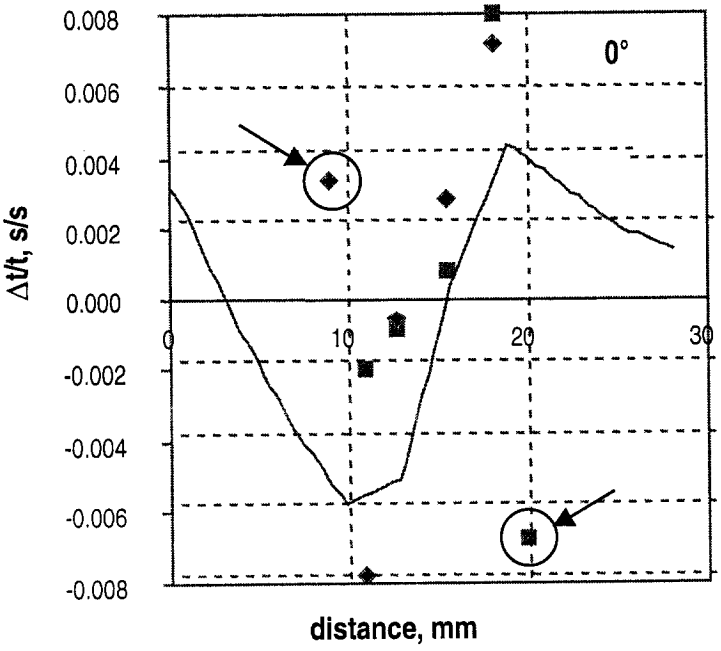

(a)

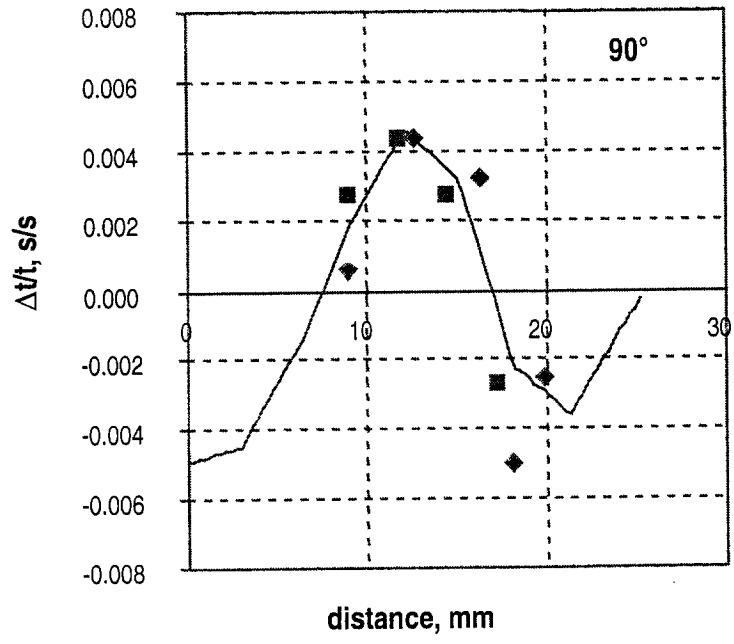

(b)

Figure 41. Experimental results and finite element calculations of a compressed ring. Symbols are experimental results, squares and diamonds represent two different measurements. Lines are from finite element calculations.

Experimental results and finite element calculations are plotted in Figure 41. The distance is measured from the inside edge, that is, distance = $r - r_i$. Experimental values were prone to error in the area close to the inside and outside edges of the ring. The curvature and boundary caused edge reflections that disturbed the waveform and resulted in inconsistent signals. It is evident that the two points circled and indicated with an arrow in the Figure 41(a) are not consistent with the rest of the data. In the center region, results are in reasonably good comparison with the finite element calculations. The 0° data (x-axis) shows a larger scatter.

Plastically Deformed Beam

A beam with a precisely known residual stress distribution was used in this experiment. The beam was very carefully prepared by Los Alamos National Laboratory. It was made of 21CR-6Ni-9Mn austenitic stainless steel and had a 30 mm by 10 mm cross section in the gauge section as shown in Figure 42. Various methods, including neutron and X-ray diffraction, had been used to measure the residual stresses. The preparation of this beam and the results of measurements were described in detail in [38].

The surface of the beam specimen was not polished. The reflected CW laser beam from the specimen was diffusive, so the two-point detection technique was not applicable. Relative TOF was measured over a fixed length of about 30 mm between the line excitation (T) and the receiving point (R) as shown in the figure. The specimen was mounted on a stage, so it's vertical position could be monitored and manually controlled by using a micrometer. All laser beams, generated from both pulsed and CW lasers, were aligned in the same horizontal plane and remained undisturbed during the experiment. During experiment, Rayleigh surface waves traveled horizontally (i.e., along the axis the beam). By moving the specimen up and down, TOF was scanned at 1.5 mm increments vertically.

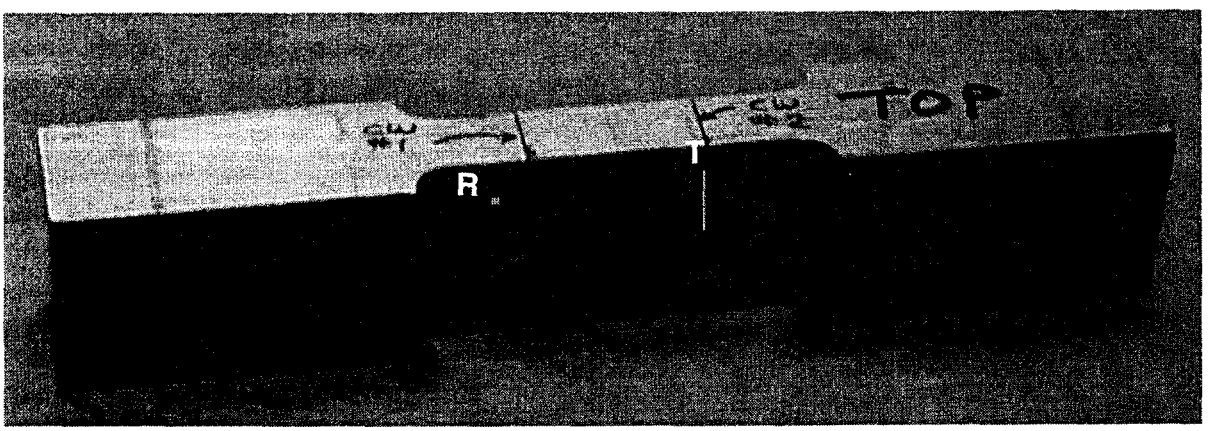

Figure 42. Beam with a precisely known residual stress distribution prepared by Los Alamos National Laboratory. R and T show the receiving and transmitting locations, respectively, for the LU measurements.

Two assumptions have been applied in analyzing neutron and X-ray diffraction data [38] and are also used here: that this is a plane stress condition ($\sigma_2 = 0$) and that σ_1 varies only vertically in the gage section. Acoustoelastic equation (1) becomes

$$\sigma_1 = (\Delta V_1 / V_1^\circ) / K_{11} = - (\Delta t_1 / t_1^\circ) / K_{11} \qquad (11)$$

If the acoustoelastic coefficient K_{11} of the material is available, the residual stress distribution can be predicted. Unfortunately, the value is not available. However, to demonstrate the LU technique, we use the acoustoelastic constants of SS304L, shown in Figure 43. The result is plotted in Figure 44. The stress distribution has a similar trend. The magnitude of the stress is not comparable since the K_{11} value is not correct; nonetheless, the stress is in the right order of magnitude.

Similar to the ring experiment described in the last section, the precision of TOF measurement decays when the measurement is close to the edge of the specimen. Such uncertainty may cause a large error in stress value; therefore, only the center section was considered. Also, TOF measurements are more difficult in steel than in aluminum since the acoustoelastic constant for steel is only about 25% that of aluminum. Repeating this experiment with an aluminum beam would be useful.

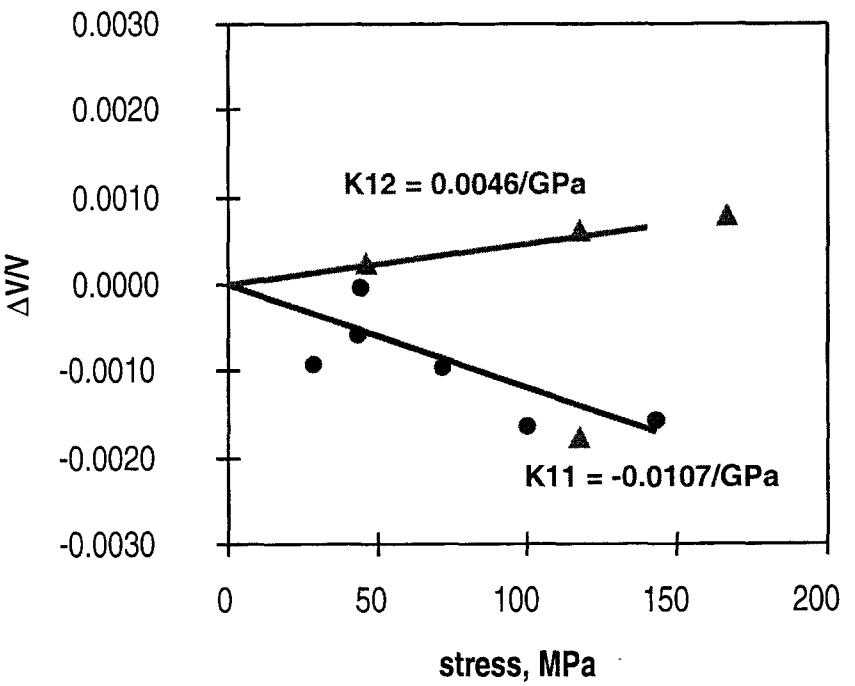

Figure 43. Acoustoelastic coefficient of SS304L.

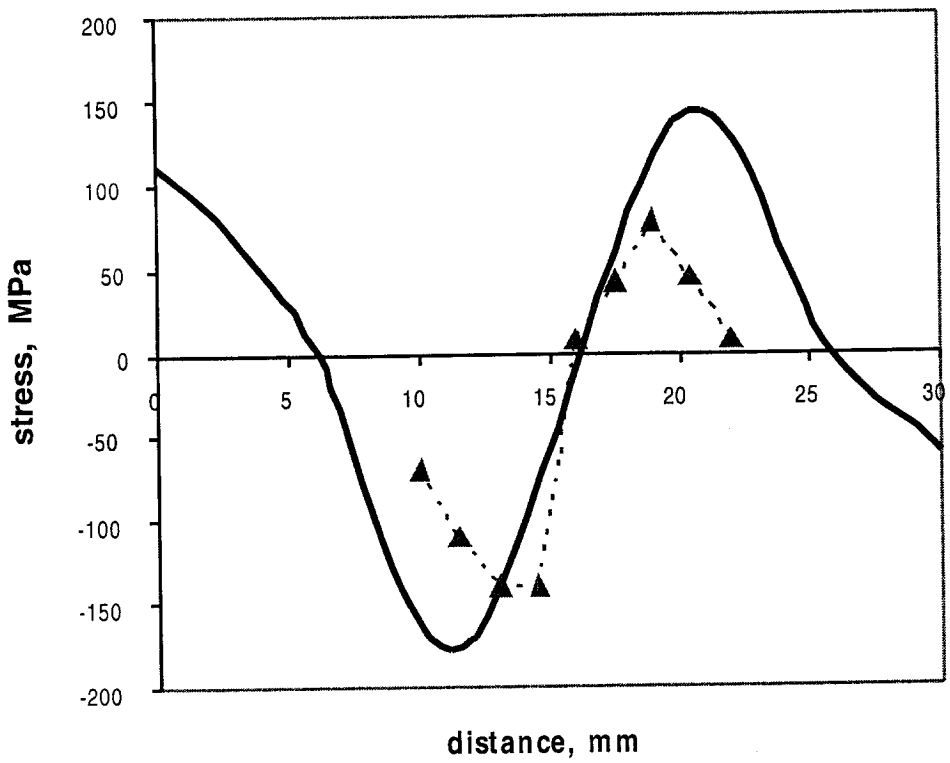

Figure 44. LU measured (triangles) and known (line) residual stress profile starting from the top of the beam.

Welded Pipe

As shown in Figure 45, we have attempted stress measurement on a welded aluminum pipe. Since the stresses are very important to any sort of failure prediction for the welded joint, it is desirable to know the stresses on the inside and outside surfaces of the pipe. It is difficult to make x-ray measurements inside the pipe. The use of neutron diffraction measurements is questionable, as the pipe is about 2.4 mm thick, and the smallest volumes that the neutron technique can measure are 1x1x1 mm^3 or a 0.6x0.6x10 mm^3 'matchstick' volume. If the laser ultrasonic technique was currently fully developed, it could be used for this application because of its capability in stress gradient measurement.

Although we were able to generate narrow band waveforms from a pulsed laser source, we were not able to obtain consistent and accurate velocity versus frequency relations. Piezoelectric transducers were not applicable because of geometric constraints.

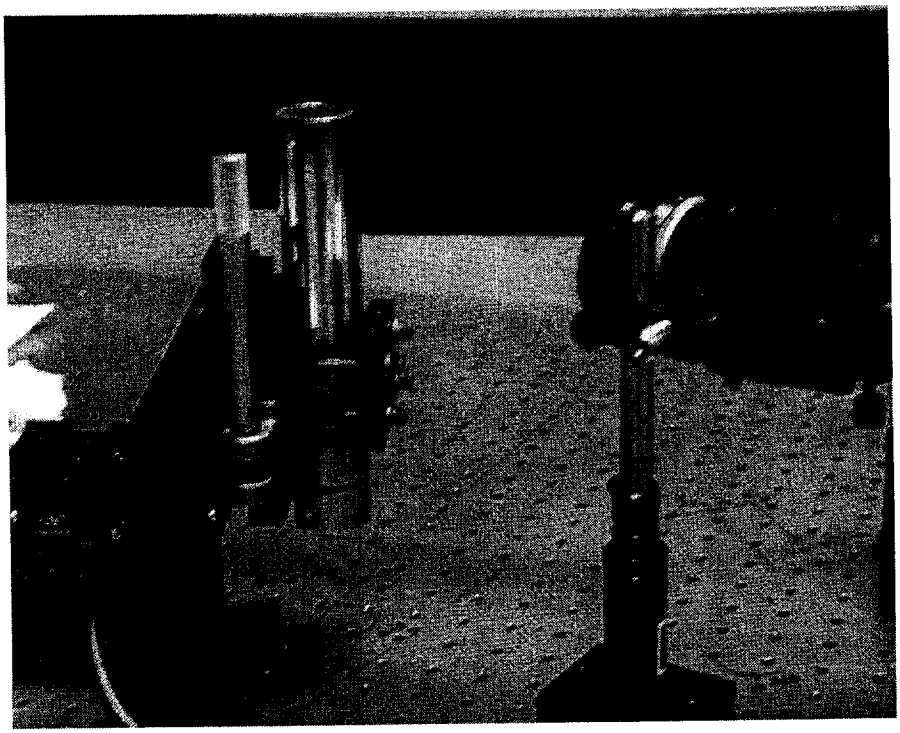

Figure 45. An attempted LU measurement on a welded pipe.

Discussions on Resolution and Accuracy of Measurements

Acoustoelastic Coefficients

The sensitivity of ultrasonic stress evaluation depends on the magnitude of acoustoelastic coefficients, which vary from material to material and the direction of measurement. Comparing the two materials we have measured during the investigation utilizing Rayleigh waves, for example, Al6061-T6 (K_{11} = - 0.022 GPa^{-1}) is twice as sensitive as SS304L (K_{11} = - 0.0107 GPa^{-1}); and for both materials, TOF measured along the direction of traction is more than twice as sensitive to stress as measured in the transverse direction.

Texture

The value of K_{11} for Al6061-T6 has been measured by other researchers using different techniques. As listed in Table 2, the value could vary in a range of ±20%. Texture may be a major factor of this scatter. Calibration of K_{11} using the same material will improve the accuracy of stress evaluation.

TOF Resolution

In LU stress measurement, the actual quantity measured is TOF. The resolution of TOF depends on the signal-to-noise ratio (S/N) of a signal and signal processing method. The S/N of a single-shot LU signal is typically low (S/N < 3). A large number

of averaging is required to increase the signal-to-noise ratio. For example, S/N improves to ≈10 when averaging over 50 single-shot signals. Cross correlation technique is an effective method to determine TOF accurately from a signal. In our experiment the resolution of TOF is estimated to be better than ±1 ns. TOF measurement can be improved with better equipment (lasers and digitizer).

Spatial Resolution

From acoustoelastic equation (1), the change of stress ($\Delta\sigma$) is proportional to the relative change of TOF ($\Delta t / t^{\circ}$). Since the resolution of TOF is constant, the error in stress is then proportional to $(t^{\circ})^{-1}$. That means the error of stress measurement is larger when t° is shorter, or the path length is shorter. In general, if the resolution of TOF is constant, the spatial resolution and stress resolution will not improve at the same time. It is important to select an optimum path length.

Consider a path length of 1 cm. The Rayleigh wave velocity of aluminum or steel is about 3,000 m/s, so the value of t° is about 3.3 μs. Therefore, the best accuracy of stress measurement is about ±15 MPa for aluminum and ±30 MPa for steel, when Rayleigh wave propagates along the direction of traction; and it would be ±30 MPa for aluminum and ±60 MPa for steel when Rayleigh wave propagates in the transverse direction. If the path length is doubled, the error will reduce by half. These values are consistent with the experimental results shown in Figures 16 and 43, where we estimate the resolution is about ±40 MPa.

Geometry

Experimental results usually have a larger error. In addition to the limitation of TOF, the dimensional accuracy of the mechanical scan or loading device is the major source of error. For example, if the specimen rotates an angle $\theta = 1.4$ degrees, which is hardly noticed by a naked eye, the path length may change 0.03% (Figure 46). It is equivalent to a 1 ns error in TOF measurement. To obtain a good stress evaluation, the geometry of the experimental setup and the positional accuracy and consistency are extremely important.

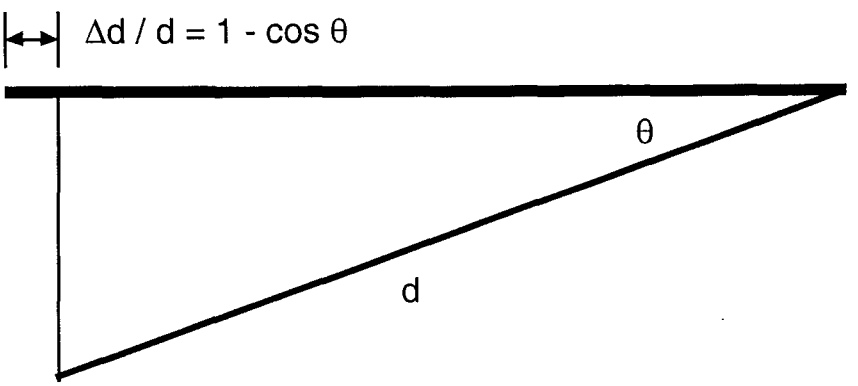

Figure 46. An unnoticed geometrical change influences the accuracy of relative TOF measurement.

Conclusion

In summary, we have developed and demonstrated a LU technique for stress measurement and a partial LU method for stress gradient measurement. The spatial resolution of the technique is about 1 cm; the stress and stress gradient resolutions are about 40 MPa and 40 MPa/mm, respectively.

A model was developed by Professor Man to include texture effects on acoustoelastic constants of aluminum alloys, which are functions of seven texture coefficients (W400, W420, W440, W600, W620, W640, and W660). Acoustoelastic constants and texture coefficients of two AA6061-T6 samples were experimentally measured. Model-predicted acoustoelastic constants from texture coefficients are in accordance with experimental values. This explains why inconsistent values were reported in the literature.

The finite element model (FEM) was validated by comparing with analytical results; which was further improved to include temperature dependent thermal and mechanical (elastic and plastic) properties of the material. Temperature dependent properties significantly decreased the peak magnitudes in waveform; including plasticity effected the shape of the waveform. FEM was used to simulate several experimental scenarios. The purpose was to guide experiments to generate desired waveforms, broadband or narrow-band signals, and for stress gradient evaluation. The effect of pulse laser spot size was investigated. It shows that frequency content of a signal increases as the source diameter decreases. Narrow-band generation was simulated by using multiple exciting sources. Increasing the number of sources with source spacing fixed narrows the bandwidth of the received waveform. FEM was also used for structural analysis for validation purposes. The stress distributions of a compressed ring and a welded tube were calculated, which would be used to compare with measured values.

Ultrasonic stress gradient measurement was demonstrated by using a piezoelectric transducer for excitation and laser ultrasonics for receiving. To have a fully LU system, the critical task is to generate desired waveforms using laser. From the guidance of FEM, we have successfully developed the technique to generate narrow band signals. Unfortunately, there are still a few problems to overcome to meet the consistency and accuracy required for velocity measurement.

The applicability of LU techniques were demonstrated by three experiments. First, an annular ring made of AA6061-T6 was compressed diametrically beyond yield. The residual stress distribution at the horizontal section was measured, which compared well with analytical predictions. Second, LU measurements were made on a bend beam prepared by Los Alamos National Laboratory. The residual stress had been evaluated by several different techniques such as neutron and X-ray diffraction. LU results matched other results only qualitatively since the acoustoelastic constants of the material were not available. The third experiment was the weld tube. LU measurements were made; however, as mentioned above, we were not able to obtain consistent and accurate velocity versus frequency relations.

References

1. M. Hirao, H. Fukuoka and K. Hori, J. Appl. Mech., vol. 48, 119 (1981).
2. K. Jassby and D. Kishoni, Experimental Mechanics, 74 (1983).
3. G.S. Kino, D. Husson and S.D. Bennett, in *New Procedures in Nondestructive Testing,* ed. P. Holler (Springer-Verlag, New York, 1983), p. 521.
4. P.P. Delsanto, R.B. Mignogna, A.V. Clark Jr., J. Acoustic Soc. Am., 87(1), 215 (1990).
5. E.A. Lindgren, T.S. Jones, H. Berger and M. Rosen, in *Review of Progress in QNDE*, vol. 13, eds. D.O. Thompson and D.E. Chimenti (Plenum, New York, 1994), p.2039.
6. T. Berruti and M.M. Gola, *Material Science Forum Vols* 210-213 (1996), p. 171.
7. Y.C. Lee, J.O. Kim and J.D. Achenbach, , in *Review of Progress in QNDE*, vol. 13, 2025 (1994).
8. C.E. Duffer and C.P. Burger,in *Review of Progress in QNDE*, vol. 15, 539 (1996)
9. W-Y Lu, B. Maxfield and S. Kuramoto, "Ultrasonic Velocity Measurement by Correlation Method," Proceedings, 1990 Spring Conference on Experimental Mechanics, 279 (1990).
10. M. Okade and K. Kawashima, *Nondestructive Characterization of Materials* VII, 163 (1996).
11. G.S. Kino, D.Husson and S.D. Bennett, in *New Procedures in Nondestructive Testing*. ed. P. Holler (Springer-Verlag, New York, 1983), p.521.
12. F.G. Makhort, O.I. Gushcha, A.A. Chernoochenko, Int. Appl. Mech., 29, 915 (1993).
13. K. Jassby and D. Kishoni, Experimental Mechanics, 74 (1983).
14. K. Jassby and D. Saltoun, Materials Evaluation, 40, 198 (1982).
15. B.G. Martine, Materials Evaluation, 32, 229 (1974).
16. W-Y Lu, L.W. Peng and S. Holland, in *Review of Progress in QNDE*, vol. 17, 1643 (1998).
17. G.C. Johnson, J. Nondestructive Evaluation, 3, 1 (1982).
18. G.C. Johnson, ASME J. Appl. Mech., 52, 659 (1985).
19. G.C. Johnson and W.C. Springer, Int. J. Solids Structures, 25, 609 (1989).
20. C.-S. Man, Arch. Rational Mech. Anal. 143, 77 (1998).
21. C.-S. Man and R. Paroni, J. Elasticity 45, 91 (1996).
22. D. Royal and E. Dieulesaint, J. Acoust. Soc. Am. 76, 1434 (1987).
23. J.F. Thomas, Phys. Rev. 175, 955 (1968).
24. C.-S. Man, W-Y Lu and J. Li, to apear in *Review of Progress in QNDE*, vol. 18 (1999)

25. J. V. Candy, G. H. Thomas, D. Chinn, and J. B. Spicer, "Laser Ultrasonic Signal Processing: A Model Reference Approach", Lawrence Livermore National Laboratory Report UCRL-JC-122414, Oct. 1995.

26. J. B. Spicer, "Laser Ultrasonics in Finite Structures: Comprehensive Modeling with Supporting Experiment", Ph.D. Thesis, The Johns Hopkins University, 1991.

27. C. Suh, "Numerical Modeling of Laser Ultrasonic Waves using Finite Element Method and Fast Integral Wavelet Transform", Ph.D. Thesis, Texas A&M University, 1997.

28. T. M. Sanderson, "Thermoelastic Modeling of Laser-Generated Ultrasound for Nondestructive Materials Testing", Ph.D. Thesis, Georgia Institute of Technology, 1997.

29. ABAQUS/Explicit and ABAQUS/Standard, Version 5.7, Hibbitt, Karlsson & Sorensen, Inc.

30. L. M. Taylor and D. P. Flanagan, "PRONTO 2D A Two-Dimensional Transient Solid Dynamics Program", Sandia National Laboratories Report SAND86-0594, 1995.

31. G. T. Martin and H. F. Bowman, Int. Comm. Heat Mass Transfer 17, 93 (1990).

32. D. K. Gartling and R. E. Hogan, "Coyote II - A Finite Element Computer Program for Nonlinear Heat Conduction Problems, Part II - User's Manual", Sandia National Laboratories Report SAND94-1179, 1994.

33. J. M. Hicks, L. E. Urbach, E. W. Plummer, and H. Dai, Physical Review Letters 61(2), 2588 (1988).

34. D. K. Gartling, "MERLIN II – A Computer Program to Transfer Solution Data between Finite Element Meshes", Sandia Report SAND89-2989, 1991.

35. I. Stakgold, "Green's Functions and Boundary Value Problems", John Wiley & Sons, p. 134, 1979.

36. C. S. Man, Inv. Prob., 14, p. 313 (1998).

37. J. J. Dike, "An Acoustoelastic Technique Using Longitudinal Waves for the Evaluation of Residual Stresses", Ph.D. thesis, University of California, Berkeley, 1989.

38. M.B. Prime, P. Rangaswamy, M.R. Daymond and T.G. Abeln, "Several Methods Applied to Measuring Residual Stress in a Known Specimen", SEM Spring Conference on Experimental and Applied Mechanics, p. 497 (1998).

DISTRIBUTION:

Partha Rangaswamy
Los Alamos National Laboratory
MST-8, H 805
Ta 53, Bldg 622, DP 01U
Lujan Center, LANSCE 12
Los Alamos, NM 87545

Chi-Sing Man
University of Kentucky
Department of Mathematics
Lexington, KY 40506

George Johnson
University of California – Berkeley
Department of Mechanical Engineering
Berkeley, CA 94720

1	MS 0337	R. D. Skocypec (9002)
1	MS 0615	J. H. Gieske (9133)
1	MS 0841	P. J. Hommert (9100)
1	MS 1130	R. A. Neiser (1831)
1	MS 1153	F. J. Zutavern (9331)
1	MS 9042	W. A. Kawahara (8746)
10	MS 9042	W. Lu (8746)
5	MS 9042	J. J. Dike (8743)
1	MS 9102	M. W. Perra (8402)
1	MS 9108	E. T. Cull (8414)
1	MS 9402	C. M. Hartwig (8701)
5	MS 9403	L. W. Peng (8713)
5	MS 9403	J. C. F. Wang (8713)
1	MS 9405	P. E. Nielan (8743)
1	MS 9405	T. M. Dyer (8700)
3	MS 9018	Central Technical Files, 8940-2
1	MS 0899	Technical Library, 4916
1	MS 9021	Technical Communications Department, 8815/Technical Library, MS 0899, 4916
1	MS 9021	Technical Communications Department, 8815 for DOE/OSTI
1	MS 0188	D. Chavez, LDRD Office, 4001

This page intentionally left blank